The role of microstructure for crack propagation in cortical bone

Gustafsson, Anna

2019

Document Version:
Publisher's PDF, also known as Version of record

The role of microstructure for crack propagation in cortical bone

Anna Gustafsson

LUND
UNIVERSITY

DOCTORAL DISSERTATION

by due permission of the Faculty of Engineering, Lund University, Sweden.
To be defended in Segerfalksalen BMC A10, Sölvegatan 17, Lund

December 10th 2019 at 09.15

Faculty opponent
Professor Bjørn Helge Skallerud

Cover artwork by Anna Gustafsson showing the vascular microstructure of bovine cortical bone. The colors represent the angular orientation of the microstructure.

Department of Biomedical Engineering
Lund University
P.O. Box 118, SE-221 00 Lund
Sweden

ISBN: 978-91-7895-342-4 (print)

ISBN: 978-91-7895-343-1 (pdf)

ISRN-nr: LUTEDX/TEEM – 1121 – SE

Report No. 6/19

Printed in November 2019 by Tryckeriet i E-huset, Lund, Sweden

Public defence

December 10th, 2019, 09.15 in Segerfalksalen
BMC A10, Sölvegatan 17, 222 42 Lund, Sweden

Supervisors

Prof. Hanna Isaksson
Department of Biomedical Engineering, Lund University

Prof. Mathias Wallin
Division of Solid Mechanics, Lund University

Dr. Hanifeh Khayyeri
Department of Biomedical Engineering, Lund University

Faculty opponent

Prof. Bjørn Helge Skallerud
Department of Structural Engineering
Norwegian University of Science and Technology, Trondheim, Norway

Board of examination

Prof. Cecilia Persson
Department of Engineering Sciences, Applied Materials Science
Uppsala University, Uppsala, Sweden

Prof. Jonas Stålhand
Department of Management and Engineering, Division of Mechanics
Linköping University, Linköping, Sweden

Assoc. Prof. Lisa Prahl Wittberg
Department of Mechanics
Royal Institute of Technology (KTH), Stockholm, Sweden

Deputy member: Assoc. Prof. Christina Bjerkén
Department of materials science and applied mathematics
Malmö University, Malmö, Sweden

Organization LUND UNIVERSITY Department of Biomedical Engineering Box 118, 211 00 Lund, Sweden	**Document name** DOCTORAL DISSERTATION **Date of issue** December 10, 2019
Author: Anna Gustafsson	Sponsoring organization

Title: The role of microstructure for crack propagation in cortical bone

Abstract

Healthy cortical bone tissue is both tough and strong and has a unique ability to resist fracture. One reason is the hierarchical structure of the tissue where toughening mechanisms at all length scales act to slow down or stop a propagating crack. The most potent toughening mechanisms arise at the microscale when cracks interact with the osteonal microstructure and deflect along weak interfaces. However, cortical bone is a living material and the tissue properties change over time. With aging the properties are known to deteriorate. Yet, the link between age-related structural and compositional changes and impaired fracture resistance in old bone is not fully known. This is key for understanding and being able to predict the increased risk for fracture with age and in patients with osteoporosis.

The aim of this thesis is to understand the role of microstructure for crack propagation in cortical bone. Both experimental and numerical techniques have been used to evaluate the importance of mechanical properties and microstructural distributions for how cracks interact with the microstructure. In the experimental part, in situ loading in combination with digital image correlation and small- or wide-angle x-ray scattering was used to simultaneously measure deformation at meso- and nanoscale in cortical bone. Micro-CT analysis of the bone samples was performed after the tests and showed that the crack trajectory to a large extent followed the microstructure. In the numerical part, the extended finite element method (XFEM) was adopted to explicitly simulate crack propagation in cortical bone at the microscale. The key feature is a new interface damage model in 2D that captures crack deflections at osteon boundaries, as seen in experiments and which previous XFEM models were not able to predict. The modelling framework has been applied to simplified geometries comprising one osteon with different orientations to look at the effect of the microstructural distribution. These models have also been used in a parameter study to identify important material properties for the fracture behavior using a statistical framework with a Design of Experiments approach. The results identified factors related to the cement line to influence the crack propagation, where the interface strength was important for the ability to deflect cracks. Furthermore, the results illustrated how reduced matrix toughness promoted crack penetration of the cement line. However, the cement line properties are not well determined experimentally and need to be better characterized. Additionally, the models have been applied to more realistic scenarios, where crack paths were simulated in microstructural geometries based on microscopy images of cortical bone. The aim was to mimic the aging process in cortical bone and investigate how increased porosity and reduced fracture energy in the tissue influenced the fracture behavior. Both factors resulted in straighter crack paths with cracks penetrating osteons, similar to what is seen experimentally for old cortical bone. However, only the latter predicted a more brittle failure behavior. In the final study, the interface model was applied at the mesoscale to simulate crack propagation in larger domains compared to the previous models. In this case, orientation maps based on micro-CT images from the experimental study were converted to FE-models to introduce the microstructure in the models. The simulated crack paths captured the trends seen in experiments with more irregular cracks predicted for crack propagation perpendicular to the osteon orientation.

In summary, the work in this thesis illustrates the important role of cortical bone microstructure in providing alternative crack paths in the tissue. It also highlights the need of techniques to study local damage both in experimental and numerical settings, and the gain of using computational models as complementary methods to experimental techniques to identify and distinguish effects of different damage mechanisms in cortical bone.

Key words: crack deflection, interface, mechanical test, micro-CT, osteon, porosity, XFEM

Classification system and/or index terms (if any)

Supplementary bibliographical information ISRN: LUTEDX/TEEM – 1121 – SE Report No. 6/19	**Language:** English
	ISBN: 978-91-7895-342-4 (print) ISBN: 978-91-7895-343-1 (pdf)
Recipient's notes	**Number of pages** 178 / Price
	Security classification

Signature:  Date: 2019-10-29

Populärvetenskaplig sammanfattning

Frisk benvävnad har en unik förmåga att stå emot belastning utan att gå sönder, men när skelettet åldras eller påverkas av sjukdom, till exempel benskörhet, minskar benets styrka och risken för frakturer ökar. En fraktur börjar som en liten spricka innuti benvävnaden som utvecklas till en fullskalig fraktur om belastningen blir för hög, till exempel vid ett fall. Därför är det viktigt att förstå hur dessa mikroskopiska sprickor växer genom benvävnaden och hur sättet sprickorna växer på förändras när benvävndaden drabbas av sjukdom.

De unika egenskaperna hos frisk benvävnad kommer från dess specifika uppbyggnad. På nanoskala blandas byggstenar av mjukt och flexibelt kollagen med hårda mineralkristaller. På lite större skala (mikroskala) kan benvävnad liknas vid armerad betong, där rörliknande strukturer, så kallade osteoner, utgör armeringen. Osteonerna är omgivna av tunna skikt som kallas för cementlinjer. Dessa består av ett sprött material och utgör svaga strukturer i benvävnaden. Experiment visar att just cementlinjerna har stor betydelse för vilken väg en spricka färdas genom benvävnaden eftersom sprickor tenderar att följa svaga strukturer. Beroende på vilken riktning sprickan har gentemot osteonerna så kommer sprickvägen genom benet se väldigt olika ut. Om sprickan färdas längs med osteonerna får man en jämn spricka, men om sprickan färdas vinkelrätt mot osteonerna blir sprickan ojämn eftersom den byter riktning när den viker av längs cementlinjerna. Ett material med ojämna sprickor är mer motståndskraftigt mot brott, eftersom sprickorna bromsas upp när de byter riktning och en längre spricka kräver mer energi för att bildas. Det här doktorandprojektet gick ut på att, utifrån ett ingenjörsperspektiv, förstå hur sprickor i ben uppstår och växer. Främst var målet att förstå hur benvävnadens riktning och arkitektur påverkar vilken väg sprickor färdas genom materialet samt hur detta påverkar förmågan att stå emot belastning.

Datormodeller i kombination med experiment och högupplöst avbildning (datortomografi) användes i forskningsprojektet för att studera sprickor i kompakt benvävnad med teorier och verktyg hämtade från fält som materialvetenskap och mekanik.

I den första studien belastades benprover tagna från kor och sprickvägen genom materialet jämfördes med benvävnadens struktur. Högupplösta bilder visade hur sprickorna följde mikrostrukturen. En viktig del av forskningsprojektet var att utveckla en datormodell som kunde förutspå realistiska sprickvägar med sprickor som vek av längs svaga gränsskikt. Den möjligheten saknades i tidigare modeller, där sprickor istället alltid förutspåddes fortsätta växa rakt fram genom osteoner utan att påverkas av cementlinjen. Arbetet med modellutvecklingen presenteras i studie II.

En datormodell bygger på ett antal parametrar eller värden, och dessa behöver mätas och bestämmas med hjälp av experiment. I många situationer är det omöjligt att genomföra dessa mätningar och då kan istället datormodeller användas för att testa ett stort antal olika hypotetiska värden och se vad de får för effekt. Detta tillvägagångssätt användes i studie III, där modellen från studie II användes för att kartlägga vilka parametrar som hade stort inflytande på sprickan och hur olika kombinationer av parametrar gav upphov till olika typer av sprickvägar. Resultaten visade att ju svagare cementlinjen var desto större var chansen att sprickan vek av längs den, samt att kvaliteten i det omgivande materialet hade stor betydelse för om sprickan skulle vika av eller ej.

Studier i litteraturen visar att frakturer hos äldre eller bensköra personer ofta har mycket rakare sprickor jämfört med yngre personer. Dock är de bakomliggande orsakerna till stor del okända. I studie IV fokuserades därför arbetet på att förstå hur två åldersrelaterade förändringar i benvävnad påverkar sprickvägen och därmed motståndskraften mot frakturer. Dessa var porositet och materialkvalitet. Att gammalt ben är mer poröst än ungt ben är välkänt och har länge ansetts vara anledningen till risken för fraktur ökar med åldern. Resultaten visade dock att endast ökad porositet inte kan förklara den ökade risken för fraktur utan att även förändringar i benvävnaden (materialet som finns kvar mellan porerna) krävs. Datormodellerna visade att både ökad porositet och försämrad materialkvalitet orsakar rakare sprickvägar och att en kombination av båda faktorerna troligen ligger bakom den ökade frakturrisken hos äldre.

Datormodeller kräver alltid en rad förenklingar jämfört med hur verkligheten ser ut. Ett sådant exempel är beskrivningen av osteonerna i studie II-IV, där de beskrevs av enkla geometriska figurer såsom cirklar och ellipser. I studie V skapades en mer realistisk beskrivning av mikrostrukturen genom att utgå från högupplösta datortomografibilder av benprover som testats experimentellt i studie I. Samma analyser av sprickvägar och sprickornas oregelbundenhet som genomfördes i

studie I upprepades för datormodellerna i studie V. Resultaten överensstämde väl med experimenten och kunde dessutom ge ytterligare insikt i sambandet mellan sprickväg och förmågan att stå emot fraktur.

Förhoppningen är att den här typen av datormodeller kommer kunna förklara fler av de bakomliggande orsakerna till observationer som görs experimentellt. Slutmålet i framtiden är att utröna vilka egenskaper hos ben som har betydelse för hur väl vävnaden kan stå emot brott för att till exempel kunna avgöra vilka aspekter av åldrande som medför störst frakturrisk. Om dessa kan identifieras så finns goda möjligheter att förbättra metoderna för att förutspå risken för fraktur.

Abstract

Healthy cortical bone tissue is both tough and strong and has a unique ability to resist fracture. One reason is the hierarchical structure of the tissue where toughening mechanisms at all length scales act to slow down or stop a propagating crack. The most potent toughening mechanisms arise at the microscale when cracks interact with the osteonal microstructure and deflect along weak interfaces. However, cortical bone is a living material and the tissue properties change over time. With aging the properties are known to deteriorate. Yet, the link between age-related structural and compositional changes and impaired fracture resistance in old bone is not fully known. This is key for understanding and being able to predict the increased risk for fracture with age and in patients with osteoporosis.

The aim of this thesis is to understand the role of microstructure for crack propagation in cortical bone. Both experimental and numerical techniques have been used to evaluate the importance of mechanical properties and microstructural distributions for how cracks interact with the microstructure. In the experimental part, in situ loading in combination with digital image correlation and small- or wide-angle x-ray scattering was used to simultaneously measure deformation at meso- and nanoscale in cortical bone. Micro-CT analysis of the bone samples was performed after the tests and showed that the crack trajectory to a large extent followed the microstructure. In the numerical part, the extended finite element method (XFEM) was adopted to explicitly simulate crack propagation in cortical bone at the microscale. The key feature is a new interface damage model in 2D that captures crack deflections at osteon boundaries, as seen in experiments and which previous XFEM-models were not able to predict. The modelling framework has been applied to simplified geometries comprising one osteon with different orientations to look at the effect of the microstructural distribution. These models have also been used in a parameter study to identify important material properties for the fracture behavior using a statistical framework with a Design of

Experiments approach. The results identified factors related to the cement line to influence the crack propagation, where the interface strength was important for the ability to deflect cracks. Furthermore, the results illustrated how reduced matrix toughness promoted crack penetration of the cement line. However, the cement line properties are not well determined experimentally and need to be better characterized. Additionally, the models have been applied to more realistic scenarios, where crack paths were simulated in microstructural geometries based on microscopy images of cortical bone. The aim was to mimic the aging process in cortical bone and investigate how increased porosity and reduced fracture energy in the tissue influenced the fracture behavior. Both factors resulted in straighter crack paths with cracks penetrating osteons, similar to what is seen experimentally for old cortical bone. However, only the latter predicted a more brittle failure behavior. In the final study, the interface model was applied at the mesoscale to simulate crack propagation in larger domains compared to the previous models. In this case, orientation maps based on micro-CT images from the experimental study were converted to FE-models to introduce the microstructure in the models. The simulated crack paths captured the trends seen in experiments with more irregular cracks predicted for crack propagation perpendicular to the osteon orientation.

In summary, the work in this thesis illustrates the important role of cortical bone microstructure in providing alternative crack paths in the tissue. It also highlights the need of techniques to study local damage both in experimental and numerical settings, and the gain of using computational models as complementary methods to experimental techniques to identify and distinguish effects of different damage mechanisms in cortical bone.

List of appended papers

This thesis consists of a review of the author's work in the field of biomedical engineering. The following selection of the author's publications is referred to in the text by their Roman numerals. Papers I-V are appended at the end of the thesis and have been reproduced with the permission of the copyright holders.

I. **Gustafsson, A.***, Mathavan, N.*, Turunen, M. J., Engqvist, J., Khayyeri, H., Hall, S. A., Isaksson, H. Linking multiscale deformation to microstructure in cortical bone using in situ loading, digital image correlation and synchrotron X-ray scattering. *Acta Biomaterialia, (2018), 69*, 323-331 * Joint first authors

II. **Gustafsson, A.**, Khayyeri, H., Wallin, M., Isaksson, H. An interface damage model that captures crack propagation at the microscale in cortical bone using XFEM. *Journal of the Mechanical Behavior of Biomedical Materials, (2019), 90*, 556-565

III. **Gustafsson, A.**, Wallin, M., Khayyeri, H., Isaksson, H. Crack propagation in cortical bone is affected by the characteristics of the cement line: a parameter study using an XFEM interface damage model. *Biomechanics and Modeling in Mechanobiology, (2019),* 1-15

IV. **Gustafsson, A.**, Wallin, M., Isaksson, H. Age-related properties at the microscale affect crack propagation in cortical bone. *Journal of Biomechanics, (2019),* 109326

V. **Gustafsson, A.**, Wallin, M., Isaksson, H. The influence of microstructure on crack propagation in cortical bone at the mesoscale. *(manuscript) (2019)*

In paper I, the author of this thesis analyzed the mechanical test data and performed the digital image correlation analysis. The author of this thesis was also main responsible for writing the manuscript.

In papers II-V, the author of this thesis planned the studies together with the co-authors, developed the numerical methods and was main responsible for writing the manuscripts.

Acknowledgements

First and foremost, I would like to thank my main supervisor Hanna Isaksson for your enthusiasm, patient guidance and never-ending optimism. Thank you for giving me the opportunity to work with you in the exciting field of Biomechanics and for giving me the freedom to try out my ideas. I would also like to say thank you to my co-supervisor Mathias Wallin for introducing me to the world of finite elements in my third year of engineering school. Thank you for your encouraging words and your constructive suggestions regarding my work. I also wish to give my special thanks to my co-supervisor Hanifeh Khayyeri for your support, especially during my early days as a PhD student. You challenged me to think of the bigger picture.

Thank you to all co-authors of the first study included in this thesis: Neashan, Mikael, Jonas and Steve. Mikael, thank you for interesting discussions and for introducing me to SAXS and WAXS. Jonas and Steve, thanks for the support in analyzing the DIC data and for all help imaging the samples in the 4D Imaging Lab. Furthermore, a warm thank you to all present and former members of the Biomechanics group for the nice working environment and for understanding the importance of *fika*. A few special thanks: To Lorenzo for being an important hub in the group and for always having time for big and small questions. To Sophie, for all the fun inside and outside of the office. To Joeri, for being an excellent office mate. I really appreciate getting your quick opinion on my big and small struggles. To Thomas, for your energy and for always being ready with a helping hand. To Elin, Isabella and Maria, for your positive attitudes and all the interesting discussions. Thanks to all colleagues at BME for making it such a great workplace, especially to the people in the acoustofluidics group for nice talks in the lunchroom and all the Monday cakes.

Tack för allt stöd från vänner och familj på nära håll och långt bort. Ett särskilt tack till Maja för långa luncher och härligt familjehäng, till Sara och Johan för after work med diskussioner om stort och smått och till nya och gamla körvänner för att ni förgyller min tid. Ett oändligt stort tack till Emma och Andreas för oräkneliga middagar och galna upptåg och för att ni aldrig är mer än 10 minuter bort. Tack till Adam för att du valde Skåne framför Norrland så vi fick inkludera dig i lundalivet. Tack mamma och pappa för att ni alltid finns där. Tack Andreas, du är min bästa. Utan dig hade jag aldrig kommit hela vägen fram.

List of abbreviations

ANOVA	analysis of variance
ASTM	American Society for Testing and Materials
BMD	bone mineral density
BSE	backscattered electron imaging
cl	cement line
CT	computed tomography
DIC	digital image correlation
LEFM	linear elastic fracture mechanics
mat	matrix
MAXPE	maximum principal strain (criterion)
MAXPS	maximum principal stress (criterion)
micro-CT	micro computed tomography
MTS	maximum tangential stress (criterion)
ost	osteon
QUADE	quadratic nominal strain (criterion)
QUADS	quadratic nominal stress (criterion)
R-curve	crack resistance curve
SAM	scanning acoustic microscopy

SAXS	small-angle x-ray scattering
SEM	scanning electron microscopy
SIF	stress intensity factor
TSS	total sum of squares
WAXS	wide-angle x-ray scattering
XFEM	extended finite element method

Contents

1 Introduction

Bone is a remarkable material that is tailored to carry loads without fracturing. However, aging and degenerative bone diseases, such as osteoporosis, drastically increase the risk of suffering a fracture. One in three women and one in five men over the age of 50 are estimated to sustain an osteoporotic fracture during their lifetime (Hernlund et al., 2013). In 2010, 27 million patients were estimated to have osteoporosis in the European Union and the corresponding economic burden was estimated to € 37 billion (Hernlund et al., 2013). With an aging population, these numbers are expected to increase, and osteoporotic fractures will remain a major health problem for both the individual and the society.

An efficient identification of patients at risk and suitable treatments are needed to reduce the burden from osteoporotic fractures. Osteoporosis is characterized by reduced bone mass and diagnosed based on measurements of bone mineral density (BMD) (Kanis et al., 2019). However, fracture risk prediction is a complex task that involves large uncertainties in a clinical setting. The current clinical models for risk assessment rely on BMD in combination with patient specific information, e.g. age, gender and medical history (Kanis et al., 2008). Still, the predictive capabilities of these clinical models are insufficient as only half of the patients that suffer a fracture are actually considered to be at risk (Oden et al., 2013; Wainwright et al., 2005). Additional information about bone strength based on patient specific computational models could improve the tools for fracture risk prediction (Johannesdottir et al., 2018; Viceconti et al., 2018), however, insufficient strength might not be the only mechanical reason behind a fracture (Hernandez and van der Meulen, 2017). In order to explain the possible failure mechanisms in clinically relevant fractures two additional measures, i.e. the fracture toughness and the fatigue strength, need to be considered (Hernandez and van der Meulen, 2017). The fatigue strength describes failure caused by low repetitive loading over time and is a key factor for clinical stress fractures (Acevedo

et al., 2018; Aspenberg and Schilcher, 2014; Iwamoto and Takeda, 2003; Jones et al., 2002). This type of fractures is outside the scope of this thesis. The fracture toughness describes the ability to resist crack growth and is an important parameter for materials that break from cracking rather than yielding (Taylor, 2018). This is often the case for biological materials, and low fracture toughness can explain why bones break at subcritical loads (Taylor, 2018). Hence, a better understanding of the underlying damage mechanisms in bone is key to develop reliable predictive tools for fracture risk assessment.

Both the composition and the hierarchical structure of bone need to be considered when trying to explore the origin of bone's resistance to fracture. The work presented in this thesis focuses on how growing cracks interact with the microstructure of cortical bone. Bone composition and structure provide efficient mechanisms that protect the tissue from fracturing by preventing crack nucleation and by slowing down, redirecting and hindering the growth of emerging cracks (Launey et al., 2010). Furthermore, healthy bone tissue has an excellent capability of repairing microcracks before they reach a critical size by continuously replacing damaged tissue (Taylor et al., 2007). However, in old bone tissue, these protective mechanisms seem to be impaired and the bone is more prone to fracture (Boskey and Imbert, 2017; Burr, 2019). Observations from experiments show that cracks in old bone seem to be less affected by the microstructure, and many toughening mechanisms are therefore absent, which results in straighter crack trajectories through the tissue (Koester et al., 2011; Nalla et al., 2004a; Zimmermann et al., 2015; Zimmermann et al., 2011). Exactly *what* the underlying changes are and *how* they alter the fracture behavior of old bone tissue is still largely unknown.

2 Aim and design of the study

The overall aim of this thesis is to analyze the role of microstructure for crack propagation in cortical bone using both experimental and numerical techniques.

The specific objectives are:

- **I** To investigate how the microstructure of cortical bone is related to deformation and damage at nano- and mesoscales using a multimodal experimental setup
- **II** To develop a numerical interface damage model that captures realistic crack patterns in Haversian cortical bone at the microscale
- **III** To identify the most important material parameters in the numerical model developed in **II**
- **IV** To apply the numerical model to patient specific geometries to assess the effect of porosity and material integrity on crack propagation
- **V** To develop micro-CT based models at the mesoscale in order to mimic the experimental setup and assess the effect of microstructural orientation numerically

2.1 Design of the study

The specific objectives above were addressed in five scientific studies (**I-V**), with the adopted study design visualized in Figure 2.1.

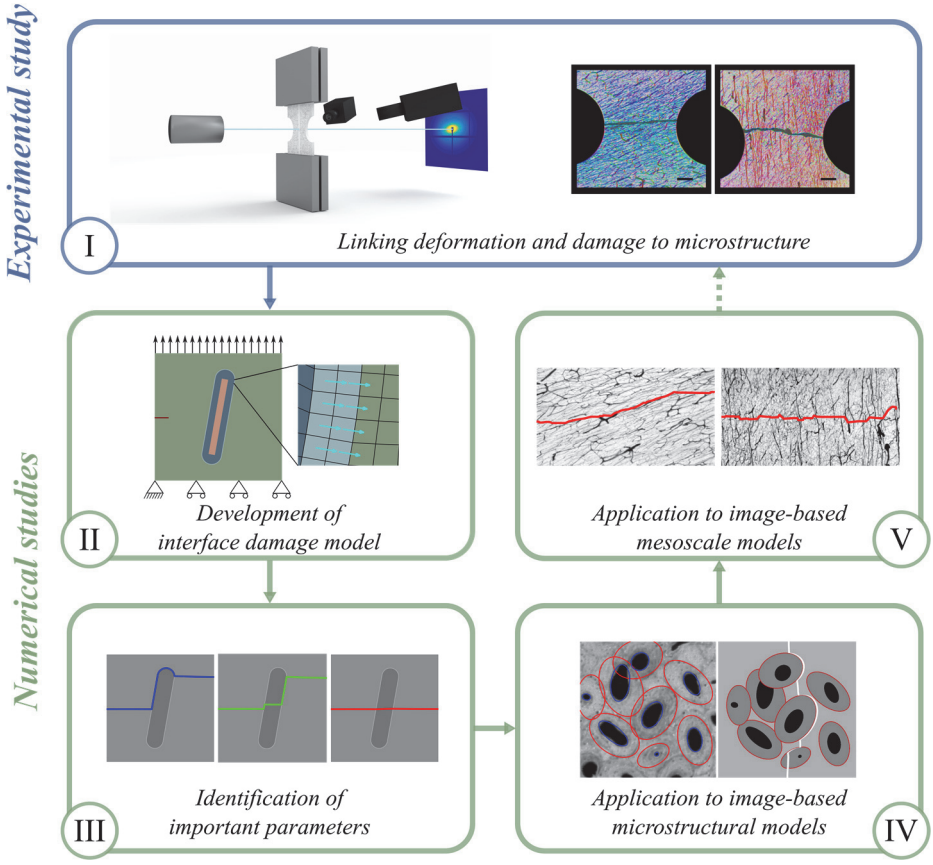

Figure 2.1. Overview of the study design. The Roman numerals I-V refer to the papers appended in the thesis and the objectives specified in section 2.

3 Background

3.1 Bone structure and composition

Bone is a composite material made up by a soft organic matrix (mostly collagen I), a stiff mineral phase (hydroxyapatite crystals) and water. These basic constituents are arranged in a well-defined hierarchical structure, where up to eleven distinct levels have been defined from the molecular building blocks up to organ scale (Reznikov et al., 2018). For many applications, it is sufficient to simplify the structure into fewer hierarchical levels and the ones relevant for the work presented in this thesis are illustrated in Figure 3.1.

At the nanoscale, tropocollagen molecules assemble in a staggered fashion into fibrils with a well-structured periodicity of 67 nm (Figure 3.1). The ends of the collagen fibrils are connected and stabilized with enzymatic cross-links (Burr, 2019). The collagen fibrils are reinforced by mineral crystals deposited both within the gaps between the collagen molecules and on the fibril surfaces and the mineral platelets are oriented parallel to the collagen fibril orientation (McNally et al., 2012). Water is found in different forms at the nanoscale, e.g. as loosely bound water molecules in the interface between collagen and minerals and as bound water within collagen molecules and mineral crystals (Burr, 2019). At the microscale, the mineralized collagen fibrils are packed into lamellar sheets that are arranged into layered plywood structures. The lamellae form two different tissues at the mesoscale: trabecular (spongy) bone and cortical (compact) bone. These two tissue types make up the whole bone at the organ scale, where cortical bone forms the hard, outer shell, whilst the porous, internal structure consists of trabecular bone. Cortical bone is also found in the shaft of long bones, e.g. in the thigh bone (lat. femur).

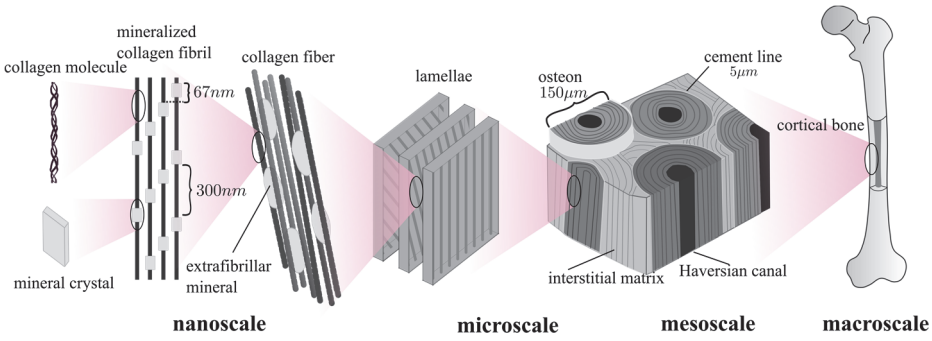

Figure 3.1. Hierarchical structure of bone showing six levels of hierarchy ranging from the macroscale down to the molecular scale.

3.1.1 Haversian bone tissue

Cortical bone can be divided into subgroups depending on the organization of the bone lamellae. A plexiform bone structure, where the lamellae are packed into larger layers, is commonly found in bovine bone (Mayya et al., 2016). In mature human cortical bone, the lamellae instead form concentric rings around the Haversian canals. These tubular lamellar structures are called osteons and they are the main structural unit of Haversian (or osteonal) bone tissue (Figure 3.1). The Haversian canals inside the osteons are the main vascular channels penetrating the compact bone tissue. Smaller channels, the so-called Volkmann canals, are oriented perpendicular to the Haversian canals and interconnect the vascular structures into a large network. The osteons are embedded in an interstitial matrix and the outer boundary is delineated with a thin interface called the cement line, which separates the osteon from the matrix. The osteons are oriented parallel to each other and run along the shaft of long bones.

The (secondary) osteon is the result of intracortical remodeling (Figure 3.2) that starts with bone-resorbing cells (osteoclasts) removing old mineralized tissue (Frost, 1969). The result is a resorption cavity that runs through the cortical bone tissue. The outer line of this cavity is referred to as the reversal surface, as this is the point where the bone resorption is reversed into bone formation (Skedros et al., 2005). Hence, the cement line (or reversal line) consists of the first material deposited on the reversal surface. This is a hyper-mineralized structure, i.e. it has a higher degree of mineralization than the matrix (Skedros et al., 2005). After the cement line has been lied down, bone-forming cells (osteoblasts), successively form the osteonal lamellae, each with a distinct fiber orientation (Wagermaier et al., 2006), until only the Haversian canal remains (Frost, 1969). The continuous remodeling process leads to a heterogenous tissue, where the degree of mineralization in each osteon is related to its age and where the surrounding

interstitial matrix is more mineralized as it consists of remnants of older osteons (Rho et al., 2002). The term targeted remodeling refers to the process where microcracks are localized and damaged tissue is repaired (Martin, 2007; Seref-Ferlengez et al., 2015).

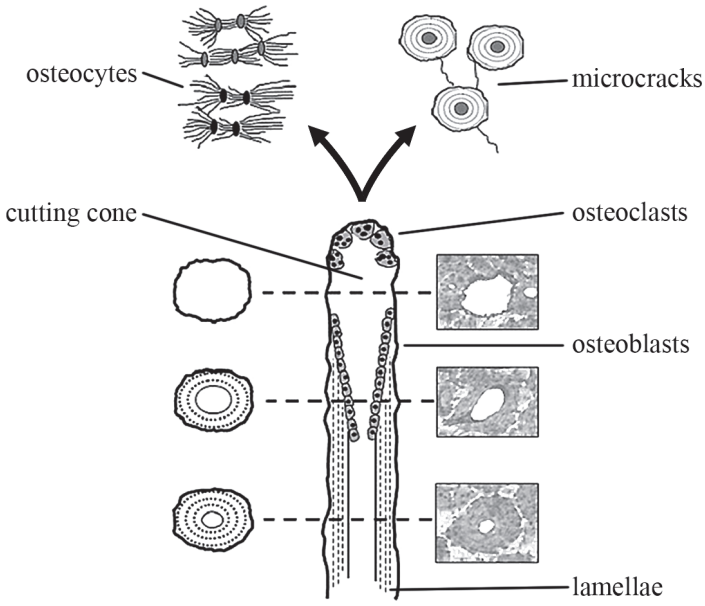

Figure 3.2. Schematic picture showing the remodeling process in cortical bone. Adapted from Fig. 1 in (Harrison and Cooper, 2015), reprinted under CC BY.

3.2 Characterization of bone mechanics

3.2.1 Mechanical testing

Mechanical tests, e.g. tensile tests, can be performed at all length scales to characterize the mechanical properties of bone (Turner and Burr, 1993). A distinction is made between structural properties that are dependent on the sample size and material properties that describe the intrinsic behavior of the material (Sharir et al., 2008). The structural properties can be determined from the force-displacement curve, where the structural stiffness is the slope in the elastic region and describes the resistance to elastic deformation. The strength describes the resistance to failure and is characterized by the peak force. The area under the force-displacement curve is a measure of the total strain energy W stored in a body and the strain energy at failure is a measure of the fracture work. The

corresponding material properties can be determined from the stress-strain curve where the material stiffness is referred to as the Young's modulus E and the material strength is expressed as either the yield strength or the ultimate strength. The toughness is a measure of the energy absorption up to failure and is calculated as the area under the stress-strain curve (Turner and Burr, 1993).

Theories from fracture mechanics are useful when looking at the resistance to crack growth. Linear elastic fracture mechanics (LEFM) is applicable to materials with no or small inelastic regions at the crack tip. Even though this is not the case for bone tissue, tools from LEFM are commonly used to characterize the fracture resistance for a given mode of loading, where mode I is tensile loading, mode II is shear loading and mode III is anti-plane shear loading. The fracture toughness K_c is a material parameter that describes the critical stress intensity factor (SIF) value for crack growth at the tip of a crack with length a. The SIF at the crack tip can be calculated for the different crack opening modes as

$$K_{I,II,III} = Q\sigma_f\sqrt{\pi a} \tag{1}$$

where σ_f is the critical stress and Q is a scalar depending on the geometry of the test specimen and the type of applied loading (mode I, II or III). Fracture toughness can also be evaluated in terms of the critical strain energy release rate G_c, which describes the energy needed per unit area to create a crack. G_c and K_c are linked through the following relation

$$G_c = \frac{{K_c}^2}{E'} \tag{2}$$

where E' is the appropriate Young's modulus ($E' = E$ for plane-stress conditions and $E' = E/(1-\nu^2)$ for plane-strain conditions). For materials with larger inelastic regions at the crack tip, measures based on non-linear fracture mechanics are required. One such measure is the critical value of the J integral, which is calculated as a surface integral enclosing the crack tip. Furthermore, crack resistance curves (or R-curves) include repeated measurements of K, G or the J integral as a function of the crack length a. The American Society of Testing and Materials (ASTM) have developed standardized protocols for determining the fracture toughness, specifying e.g. loading protocols and required dimensions of the test specimens (K_c is defined in ASTM E399 and the J integral is defined in ASTM E1820).

3.2.2 Imaging techniques

Imaging techniques are useful when characterizing geometrical parameters of bone tissue or in combination with mechanical testing to measure deformation locally at different length scales. An overview of methods relevant for the work presented in this thesis in given in Figure 3.3 and will be described briefly in the next sections.

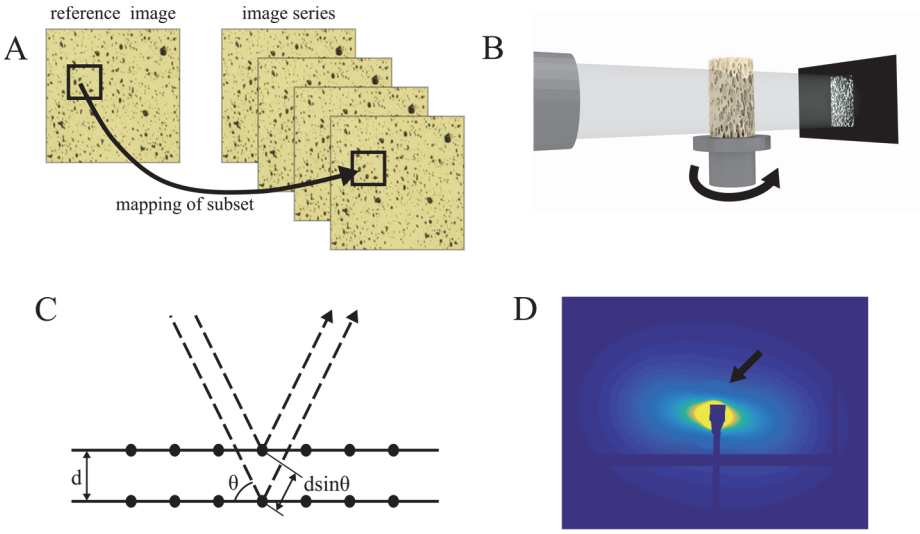

Figure 3.3. Imaging techniques used to characterize bone at different length scales. (A) The principle of digital image correlation for tracking the deformation of subsets in a series of images. (B) Computed tomography image acquisition. (C) Illustration of lattice structure for Bragg's law (equation 3). (D) A typical scattering pattern of a bone sample measured with small angle x-ray scattering. The collagen rings are indicated with a black arrow.

Digital image correlation

Digital image correlation (DIC) is a non-contact method used to calculate full-field surface strains of a tested specimen (Schreier et al., 2009). On bone it has mainly been used to analyze surface strains at the mesoscale (Grassi and Isaksson, 2015). DIC can be performed using either a single camera to measure in-plane deformations (2D DIC) or with two cameras calibrated in a stereo system to measure both out-of-plane and in-plane deformations (3D DIC). In short, a series of images is taken during a mechanical test and a tracking algorithm is used to map the reference image onto the images of the deformed specimen. The surface of the tested specimen is divided into smaller pixel subsets and these subsets are correlated to subsets on the deformed surface (Figure 3.3A). From these correlation maps,

the full displacement field can be interpolated, and the corresponding strain field can be calculated. To enhance the tracking capability, a speckle pattern is usually painted on the test specimen and the quality of the speckle pattern (e.g. speckle size, contrast etc.) in combination with the size of the subset will determine the spatial resolution of the obtained displacement field (Schreier et al., 2009).

X-ray computed tomography

X-ray computed tomography (CT) is a non-destructive imaging technique used to visualize the internal 3D structure of a sample. The sample is placed inside an x-ray beam and multiple image projections are recorded from angles between 0 and 180° (Figure 3.3B). A reconstruction algorithm is then applied to the projections to recreate a digital 3D image of the scanned sample. The intensity in the images depends on the attenuation of the x-rays passing through the sample and can be used to determine physical parameters, such as the bone mineral density or Young's modulus of bone tissue (Langer et al., 2012). CT images are commonly used in clinical practice with a resolution around 1 mm. In experimental studies, instead, high resolution micro-CT imaging is the gold standard method to visualize the 3D structure of bone with a resolution down to a few microns (Bouxsein et al., 2010; Lespessailles et al., 2006; Muller, 2009).

Small- and wide-angle x-ray scattering

A variety of x-ray diffraction techniques can be used to characterize the nanostructure of materials using Bragg's law

$$\sin\theta = \frac{n\lambda}{2d} \tag{3}$$

where 2θ is the scattering angle, λ the wavelength of the incident beam, n a positive integer and d the lattice spacing (Figure 3.3C). Bragg's law shows an inverse relationship between the size of the lattice spacing and the scattering angle. X-ray scattering techniques are commonly divided into small- and wide-angle x-ray scattering (SAXS and WAXS). These experiments prefer a well collimated beam and high flux and are therefore typically performed at synchrotron facilities. A typical scattering pattern of a bone sample measured with SAXS is shown in Figure 3.3D. The bright region in the center corresponds to scattering from the mineral crystals and the fainter rings belong to the collagen fibrils. The shape of the SAXS pattern is related to the orientation of the mineral platelets, as these scatter in the direction of their smallest dimension (Rinnerthaler et al., 1999). This can be used to estimate the predominant orientation and the degree of anisotropy at the nanoscale, where an isotropic mineral distribution would result in a circular SAXS signal (Turunen et al., 2014). SAXS scattering images can also be used to estimate

the mean crystal thickness (Rinnerthaler et al., 1999; Turunen et al., 2014). For analysis of the collagen phase, the SAXS signal is integrated radially in a sector around the predominant orientation to obtain the I(q) scattering curve, i.e. the scattering intensity as a function of the scattering vector q, where the 3rd Bragg peak corresponds to the 67 nm D-spacing in the collagen fibril (Karunaratne et al., 2013). WAXS can be used to determine the crystal length ([002] peak) and width ([310] peak) (Acerbo et al., 2014; Turunen et al., 2016) and the internal lattice spacing of the mineral crystals can be calculated from equation (3). When combined with in situ mechanical testing, strains in collagen fibrils and mineral crystals can be calculated based on the shifts in the scattering peaks measured with SAXS and WAXS (Gupta et al., 2006a; Karunaratne et al., 2013).

3.2.3 Fracture toughness of cortical bone

Bone tissue is both strong, tough and light, a combination that is rarely found in engineered materials (Wegst et al., 2015). Besides, the ability to self-heal makes healthy bone tissue tolerant to damage (Acevedo et al., 2018; Taylor et al., 2007). The unusual mechanical properties stem from the hierarchical structure of the tissue, built up by stiff and soft components, and the benefit of the composite structure can be seen when comparing the fracture toughness of the basic constituents, collagen and hydroxyapatite, to the fracture toughness of bone (Figure 3.4) (Wegst et al., 2015).

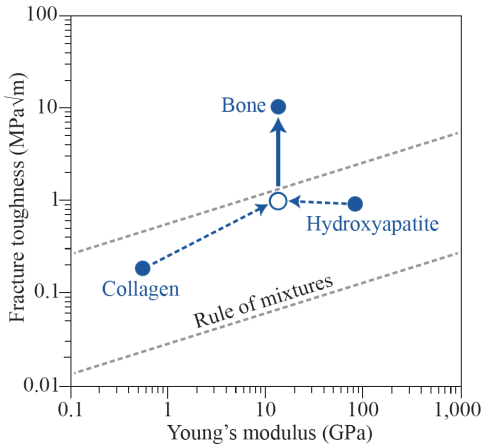

Figure 3.4. Material properties of natural composites. The fracture toughness of bone far exceeds the values of the building blocks: collagen fibers and hydroxyapatite crystals. The open ring shows the value for crack initiation and the solid ring above the solid arrow shows the crack growth toughness. Adapted from (Wegst et al., 2015) and reprinted with permission from Springer Nature.

There is a variety of toughening mechanisms active at the different length scales in bone that work to increase the tissue's resistance to fracture (Figure 3.5). Those are commonly separated into two types: *intrinsic* mechanisms found at sub-micron scales that act to prevent crack initiation and *extrinsic* toughening mechanisms typically found at the microscale that instead prevent or slow down the growth of an existing crack (Launey et al., 2010; Ritchie, 1999).

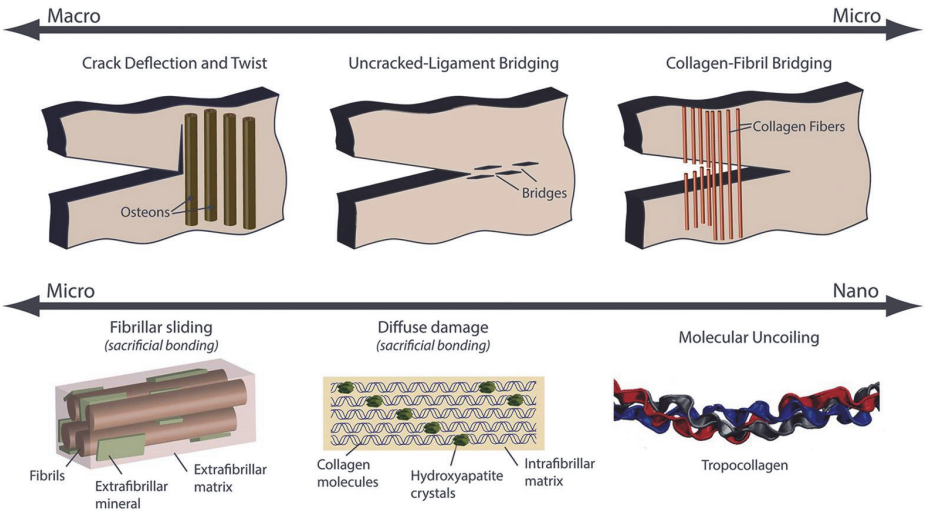

Figure 3.5. Toughening mechanisms in cortical bone at different length scales. Reprinted from Fig. 2 in (Zimmermann et al., 2015) under CC BY-NC-ND 3.0 US.

Intrinsic toughening mechanisms originate from the nanoscale and are related to the deformation of mineralized collagen fibrils. The effect of intrinsic toughening mechanisms is seen as plastic deformation at larger length scales. In the elastic loading regime, the mineralized collagen fibrils deform through stretching, however, the mineral crystals inside the collagen fibrils prevent large deformations within the collagen fibril. Interfibrillar sliding is therefore believed to be the main mechanism for plastic deformation (Zimmermann and Ritchie, 2015). This has been shown in SAXS experiments, where the strain in collagen fibrils increase linearly with tissue strain up to a certain point where the fibril strain reaches a plateau while the macroscopic tissue strain continues to increase (Gupta et al., 2006c; Zimmermann et al., 2011). Sacrificial bonds that can break and reform during deformation provide another way of dissipating energy at small length scales (Fantner et al., 2005).

Extrinsic toughening mechanisms contribute to the crack-growth resistance, which is seen as a rising R-curve behavior, and the most potent mechanisms in cortical bone are found at the microscale when a propagating crack interacts with the osteonal microstructure. Here, the cement line interfaces are important structures as they provide alternative weak crack paths that reorient the propagating crack (Lin et al., 2016; O'Brien et al., 2007; Tang et al., 2015; Zimmermann et al., 2009; Zimmermann et al., 2010). Given the importance of the microstructure, cortical bone displays highly anisotropic fracture toughness with different toughening mechanisms active for different load cases. The highest facture toughness is found in the breaking direction, i.e. when cracks propagate perpendicular to the long axis of the osteons. In this case, the crack driving force from the mechanical loading is perpendicular to the weak planes provided by the cement lines, and the competition between the two results in an irregular crack path and high resistance to fracture (Zimmermann et al., 2009). Koester et al. (2008) found the fracture toughness to be five times higher in the breaking direction, compared to the splitting direction where cracks propagated parallel to the osteons (Figure 3.6). In the splitting direction, crack bridging is the most important toughening mechanism, where intact ligaments bridge the crack (Nalla et al., 2004b). This phenomenon can also be seen as "mother and daughter cracks", where microcracks in cement lines in front of the crack tip start to grow in parallel to the main crack, leaving intact material behind in the growing crack (Launey et al., 2010). Crack bridging can also be found at smaller length scales, where instead mineralized collagen fibrils bridge the crack (Nalla et al., 2003). Katsamenis et al. (2013) found the fracture toughness in the radial direction (i.e. crack propagation in the transverse plane) to be between the two extreme cases previously described. In this direction, cracks also deflect around osteons and follow the cement lines, but the deflections are not as large as in the breaking direction and hence the increase in toughness is less pronounced.

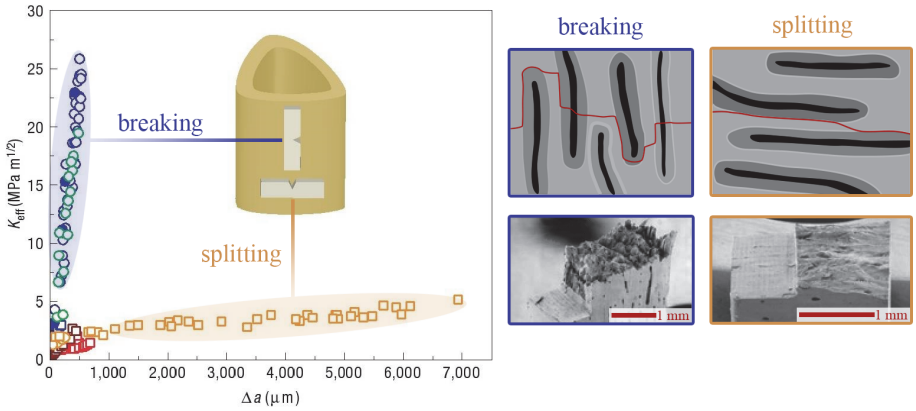

Figure 3.6. R-curves showing the difference in fracture toughness for the breaking and splitting directions of cortical bone. The crack surfaces of the tested specimens and the schematic crack trajectories illustrate how the tissue microstructure affects the crack path in the breaking (blue) and splitting (yellow) directions. Parts of the figure adapted from (Koester et al., 2008) and reprinted with permission from Springer Nature.

The conventional methods for measuring fracture toughness (i.e. according to the ASTM protocols E399 or E1820) assess the bulk properties at the tissue scale. These tests have some limitations for biological tissues. One thing is that it is often difficult to prepare test specimens of bone tissue that fulfill the ASTM standards (Taylor, 2018). Another problem is that these methods measure bulk properties and hence cannot discriminate between osteon, matrix and cement line tissues at the microscale. Mullins et al. (2009) proposed to use an indentation protocol for measuring fracture resistance at the microscale in osteon and matrix tissue. They found that longer cracks were formed in matrix tissue compared to the cracks inside osteons for equivalent indentation loads. The fracture toughness was calculated based on the indentation load, crack length and indenter geometry and was found to be highest in the osteonal tissue (Mullins et al., 2009). The use of indentation techniques to measure fracture toughness has been heavily criticized and Kruzic et al. (2009) claim in their study reviewing different indentation techniques that none of the techniques are suitable for hard biological tissue, not even for measuring the relative toughness. The technique was developed for brittle ceramic glasses and the LEFM assumptions do not hold for biological tissues as large plastic deformations occur at the crack tip where the emerging cracks are found (Kruzic et al., 2009). Kataruka et al. (2017) instead suggested to use scratch tests to assess the toughness of bone at the microscale, inspired by the Mohs hardness test that is commonly used to estimate the hardness of minerals. The main challenge with this approach is the local heterogeneity at the microscale from

the osteonal structures, which caused high variability in the results (Kataruka et al., 2017).

Characterization of the cement line

The important role of the cement line for deflecting cracks and increasing the fracture toughness of cortical bone has been shown in various studies, such as (Chan et al., 2009; Koester et al., 2008; Mohsin et al., 2006; O'Brien et al., 2005; O'Brien et al., 2007; Zimmermann et al., 2014). However, both the composition and the mechanical properties of the interface have been widely debated and this debate is still ongoing, see e.g. (Burr et al., 1988; Frasca, 1981; Milovanovic et al., 2018; Montalbano and Feng, 2011; Schaffler et al., 1987; Skedros et al., 2005).

Frasca (1981) used scanning electron microscopy (SEM) to analyze decalcified bone sections and described the cement lines as regions with amorphous ground substance, different from the collagen fiber bundles in the surrounding tissue. Burr et al. (1988) used backscattered electron (BSE) imaging and suggested that the cement line had lower mass density and reduced mineralization compared to the surrounding bone tissue. The conclusion from this study was that the cement line contained sulfated mucosubstances and thereby provided a ductile interface between the osteon and the matrix (Burr et al., 1988). More recent studies using quantitative BSE imaging (Milovanovic et al., 2018; Skedros et al., 2005) and nano-tomography (Langer et al., 2012) report that the cement lines are hyper-mineralized, i.e. have higher mineral content compared to the surrounding osteonal or matrix tissues. This was confirmed with Raman spectroscopy (Milovanovic et al., 2018). Gupta et al. (2006b) combined quantitative BSE imaging with nanoindentation and showed a correlation between mineralization and indentation modulus. However, that study was focused on determining the stiffness of the thin and thick lamellae inside the osteon and did not provide specific values for the cement line stiffness. Montalbano and Feng (2011) used nanoindentation to measure the elastic modulus of the cement line and found it to be 30% lower than the elastic modulus of the surrounding matrix tissue.

The studies mentioned so far focused on estimating the stiffness of the cement line, either directly with indentation techniques or based on mineralization data. There is, however, no consensus about the stiffness of the cement line and two opposite hypotheses prevail. One where the cement line is described as a compliant and viscous interface that attracts cracks. In this case, parallels are drawn to the nanoscale of bone and nacre where the soft collagen phase protects the stiff minerals and increases the toughness of the tissue (Montalbano and Feng, 2011). The other view describes the cement line as a stiff and brittle interface (Skedros et al., 2005). Regardless of the cement line being characterized as stiff or soft, the interface is typically described as weak (Burr et al., 1988; Montalbano and Feng,

2011; Schaffler et al., 1995; Skedros et al., 2005), and its failure properties are crucial for deflecting cracks. Dong et al. (2005) developed a protocol to perform osteon push-out tests to evaluate the debonding strength of the cement line. They showed that the cement line interface strength was approximately 10 times lower than the shear strength of osteonal lamellae (Dong et al., 2005).

The reason the cement line is weak (i.e. the preferred fracture path) compared to osteonal and matrix tissue is still not understood. Results from circular polarized light microscopy suggest that the collagen fiber orientation is different at the osteon boundary, with circumferentially oriented lamellae instead of more longitudinally oriented lamellae inside the osteons (Martin et al., 1996). More recent work using confocal laser scanning microscopy showed that the osteocyte network is disrupted at the cement lines and that the canaliculi inside the osteon follow the cement line border, creating a fine porous network along the surface (Kerschnitzki et al., 2011). This has been confirmed using nano-tomography (Langer et al., 2012) and could be relevant for the failure behavior of the interface.

In vivo, cement lines act as barriers for microcrack growth (Taylor et al., 2007). This has been quantified in vitro where fatigue tests showed that short microcracks (<100 µm) stopped at cement lines, while cracks of intermediate length deflected along the interface (Mohsin et al., 2006; O'Brien et al., 2005). Only longer cracks (>300 µm) were able to penetrate the interface and propagate through the osteon and reach the Haversian canals, and these events could lead to failure of the test specimen (Mohsin et al., 2006; O'Brien et al., 2005). Furthermore, young osteons (i.e. recently remodeled) seem more efficient in stopping intermediate and long cracks (Kennedy et al., 2008). Yeni and Norman (2000) presented an analytical model to estimate the toughness contribution from the cement line and they suggested that the weakness introduced by the Haversian canal could be compensated by the crack deflection along the cement line of the same osteon. The idea that the cement line, together with the lamellar structure inside the osteon, is protecting and shielding the Haversian canal from cracks has been supported by Wagermaier et al. (2006).

3.2.4 The effect of aging in cortical bone

Aging increases the risk for fracture (Burr, 2019; Hui et al., 1988; Melton, 1990). It is first of all due to reduced bone density (loss of bone mass), but structural and compositional changes in the bone tissue are also believed to contribute to the impaired fracture resistance (Burr, 2019). The latter characteristics are commonly referred to as bone quality (unlike bone quantity which refers only to the bone mass), and at the microscale bone quality can be described in terms of porosity,

microstructural organization, accumulated microdamage and intrinsic material properties (Boskey and Imbert, 2017; Burr, 2004; Hernandez and Keaveny, 2006).

One of the most obvious structural changes with age in cortical bone is the increase in porosity at the microscale (Figure 3.7) (Cooper et al., 2007; Feik et al., 1997; Malo et al., 2013; Mirzaali et al., 2016; Nirody et al., 2015; Stein et al., 1999; Zimmermann et al., 2016). This is due to a combination of an increased number of pores (Nirody et al., 2015) and interconnected pore spaces (Granke et al., 2016; Tong et al., 2015), as well as increased pore sizes (Nirody et al., 2015). Aging also leads to an increase in accumulated microdamage seen as linear microcracks in the tissue (Agnew et al., 2017; Diab and Vashishth, 2007; Zioupos, 2001). Both increased porosity and accumulated damage have been correlated to reduced fracture toughness (Granke et al., 2015; Granke et al., 2016; Zioupos, 2001). These structural changes can be explained by age-related alterations in the bone remodeling process that result in an imbalance between bone formation and bone resorption (Seref-Ferlengez et al., 2015).

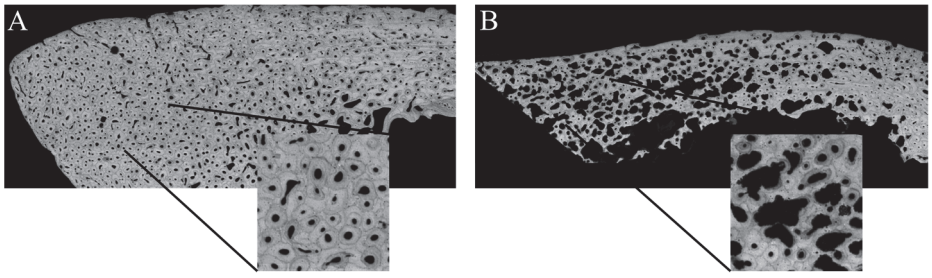

Figure 3.7. Porosity in cortical bone tissue from (A) young and (B) old donors. Image courtesy of professor K. Raum, Charité, Berlin.

There are also compositional changes with age, e.g. the formation of non-enzymatic collagen cross-links at the nanoscale (Burr, 2019; Nyman and Makowski, 2012). This type of cross-links stiffens the collagen molecules and reduces plastic deformation in the tissue by preventing sliding of the fibrils (Zimmermann et al., 2011). Furthermore, the amount of bound water in bone decreases with age, which has been correlated to decreased fracture toughness (Burr, 2019; Granke et al., 2015). Additionally, the discrepancy in mineralization between cement lines and osteons decreases with age, which could play a role in the altered crack patterns seen in old bone (Milovanovic et al., 2018).

Cracks propagating in old bone tissue are more prone to penetrate osteons. The underlying reasons are not known, but the cement line interfaces seem less capable of deflecting incoming cracks in old compared to young bone (Chan et al., 2009;

Koester et al., 2011). Typical crack paths and R-curves comparing the fracture toughness of young and old bone tissue are shown in Figure 3.8. Reduced fracture toughness is seen for both crack initiation and crack growth for all tissue orientations, however, the effect seems less severe in the breaking direction (Chan et al., 2009; Koester et al., 2011; Nalla et al., 2006).

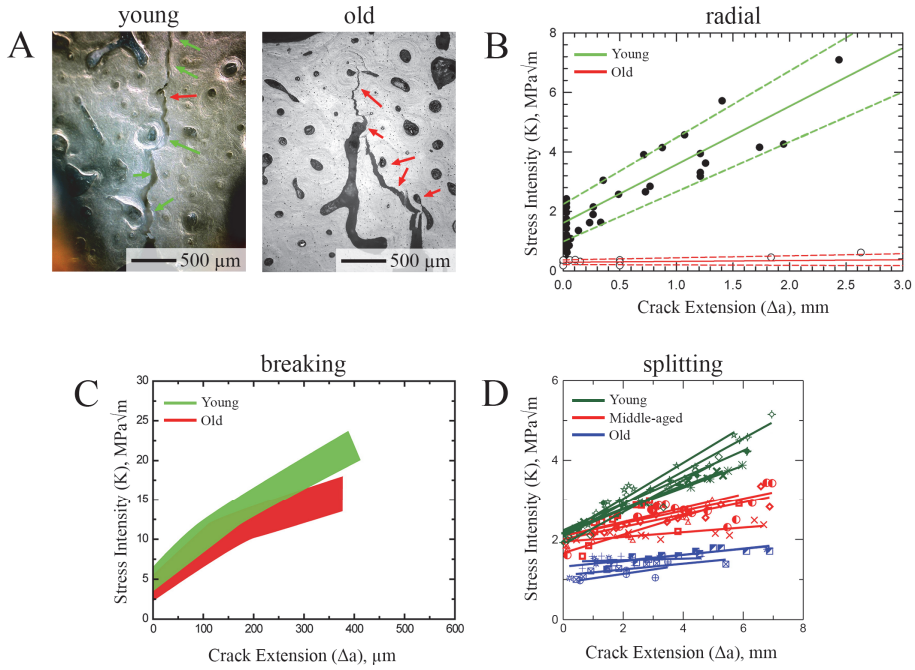

Figure 3.8. (A) Typical crack paths in young and old bone tissue. Green arrows indicate crack deflections in cement lines while red arrows show crack propagation through osteons. (B) R-curves corresponding to the samples in (A). (C) and (D) R-curves illustrating the fracture toughness in young and old bone in the breaking and splitting directions. Adapted from (Chan et al., 2009; Koester et al., 2011; Nalla et al., 2006) and reprinted with permission from Elsevier.

3.3 Damage models for bone

Numerical damage models can be divided in two main categories depending on how the crack topology is described: continuous and discrete damage models. Furthermore, two different frameworks have been traditionally used to describe damage: strength-based models, such as the Rankine criterion (Gross and Seelig, 2017) or the criterion for interface damage by Cook and Gordon (1964), and energy-based models, as the classic criteria by Griffith (1968) or the criterion for

interface damage by He and Hutchinson (1989). These two concepts, strength and energy-based failure, were combined in the cohesive damage models proposed by Barenblatt (1959).

The models commonly adopted to study bone damage will be described in the following section, together with a summary of computational studies found in literature. The description will be limited to studies using the finite element method. A more general overview of computational methods for fracture can be found in (Rabczuk, 2013) and of bone damage models in particular in (Sabet et al., 2016).

3.3.1 Continuum damage models

In continuum damage models, a smeared damage approach is used to describe the crack and the exact crack topology is not considered.

Scalar damage models

Damage can be described in different ways, and one choice is to consider a damage variable D that describes the fraction between damaged and intact material in a cross-section of a damaged body (Figure 3.9A). When D=0, the body is intact and when D=1 the body is completely damaged (Gross and Seelig, 2017). The simplest constitutive stress-strain relationship can be written as

$$\sigma = (1 - D)E\varepsilon \tag{4}$$

where E is the Young's modulus (Figure 3.9B). Damage is thereby interpreted as a decrease in stiffness and for isotropic damage D is a scalar. The initiation and evolution of damage is described by a damage law, e.g. in a general power law form:

$$\begin{cases} D = 0 & ; \varepsilon_{eq} \leq \varepsilon_c \\ D = \alpha D_C \varepsilon_{eq}^n & ; \varepsilon_c < \varepsilon_{eq} < \varepsilon_f \\ D = D_C & ; \varepsilon_{eq} \geq \varepsilon_f \end{cases} \tag{5}$$

where ε_{eq} is the equivalent strain of choice, D_C the critical damage at fracture and α and n are damage parameters that need to be determined from experiments. In a simplified version of equation (5), a finite element is immediately considered as failed once the equivalent strain reaches the failure strain

$$\begin{cases} D = 0 & ; \varepsilon_{eq} < \varepsilon_f \\ D = D_C & ; \varepsilon_{eq} \geq \varepsilon_f \end{cases} \tag{6}$$

This technique is commonly referred to as element deletion or the 'kill element' method. In practice, D_C is often chosen to be <1 so that failed elements keep a small percentage (typically around 5%) of their initial stiffness to avoid numerical difficulties. The main problem with this method is its mesh sensitivity as the localization of damage depends on the size of the finite elements and the dissipated energy is reduced when the mesh is refined (Brekelmans and Devree, 1995). The mesh-dependency can be mitigated by using suitable regularization techniques, e.g. by introducing a characteristic length in a non-local damage formulation (Brekelmans and Devree, 1995; Khoei, 2014).

Element deletion methods have been used to simulate bone strength and fracture patterns at the organ scale in the proximal femur using 2D projection models (Bettamer et al., 2017; Hambli et al., 2012) and full 3D models (Haider et al., 2018; Hambli, 2013; Marco et al., 2019; Marco et al., 2018b) (Figure 3.10A). At the microscale, Giner et al. (2017) simulated crack propagation around osteons in cortical bone to estimate the critical energy release rate of the cement line (Figure 3.10B). Furthermore, Donaldson et al. (2014) used element deletion with stress or stress-gradient based damage laws to evaluate the effect of micro porosity in the cortex of mouse femora.

The main benefit with the method is that it is easy to implement and calibrate to experiments. However, the material softening from the stiffness degradation tends to cause numerical convergence problems, which makes it challenging to capture the full crack pattern, as in (Haider et al., 2018). Furthermore, unrealistic crack paths that are highly dependent on the mesh structure and element alignment can be achieved and care must be taken to reduce such effects (Donaldson et al., 2014).

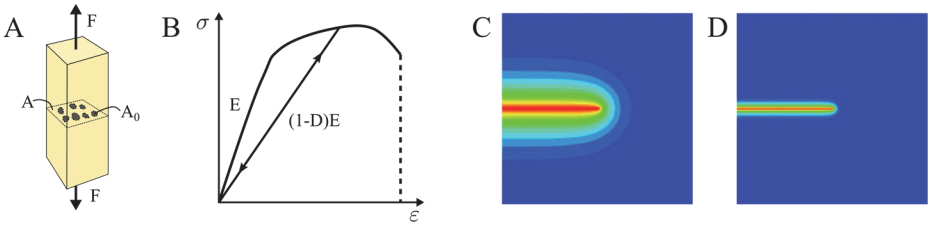

Figure 3.9. Continuum damage models. (A) Definition of damage. (B) Damage evolution. (C) Illustration of damage field in a phase-field model where blue corresponds to undamaged material and red to completely damaged material. The crack is regularized over a characteristic length and a smaller characteristic length, as in (D), gives a sharper representation of the crack. Pictures in (C) and (D) are adopted from (Miehe et al., 2010) and reprinted with permission from John Wiley and Sons.

Phase-field models

Phase-field models are another type of continuum damage models that have been introduced more recently, with important works from e.g. (Bourdin et al., 2000, 2008; Miehe et al., 2010). The basic idea goes back to Griffith's theory for brittle fracture in solids, which states that a crack will propagate if the energy release rate reaches a critical value. The limitation of the classical theory in predicting crack initiation is overcome in phase-field methods through variational methods on energy minimization (Bourdin et al., 2008). Besides this, no additional criteria are needed for crack propagation, branching or nucleation of new cracks. Within this framework, diffusive cracks are described by a phase-field that varies between 0 and 1 for intact and damaged material. The crack is regularized over an internal characteristic length that reduces to a sharp crack when the characteristic length goes to zero (Figure 3.9C-D). A refined mesh is hence needed to resolve the diffuse crack and, in cases where the crack path is not known a priori, adaptive remeshing can be beneficial.

Phase-field damage models is an active research field within the fracture mechanics community but has not yet been established for biomechanical applications. In literature, a handful of studies can be found that use the phase-field method to model damage in soft tissues (Gultekin et al., 2016, 2017, 2018; Raina and Miehe, 2016). There is no published study using the phase-field method to model bone fractures. However, Hansen-Dorr et al. (2019) developed a phase-field model for interface failure in composites, which is very similar to cortical bone. For this application, a special treatment was needed for regularizing the crack at the interface (Hansen-Dorr et al., 2019).

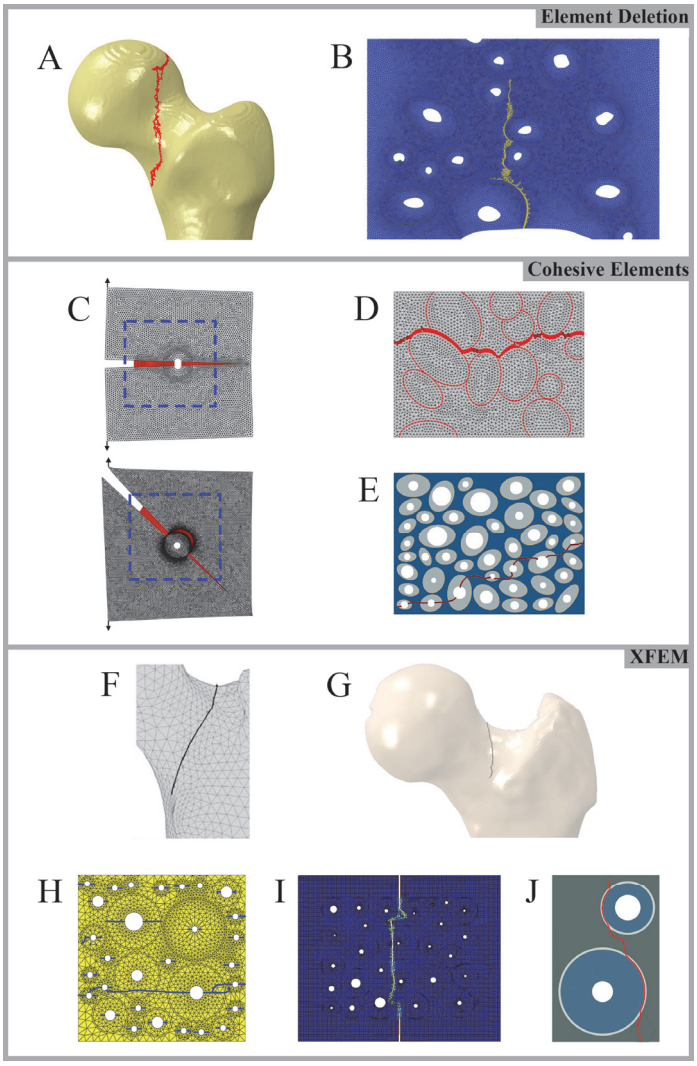

Figure 3.10. A selection of damage models presented in literature used to model crack propagation at the organ- and microscale in bone. The element deletion method used in (A) by (Marco et al., 2018b) and in (B) by (Giner et al., 2017). Cohesive elements used in (C) by (Mischinski and Ural, 2011), in (D) by (Mischinski and Ural, 2013) and in (E) by (Wang et al., 2015). XFEM used in (F) by (Gasser and Holzapfel, 2007), in (G) by (Ali et al., 2014), in (H) by (Budyn and Hoc, 2012), in (I) by (Abdel-Wahab et al., 2012) and in (J) by (Marco et al., 2018a). Figures in (A, B, G, I, J) reprinted with permission from Elsevier, (C) reprinted with permission from ASME, (D, H) reprinted with permission from Taylor & Francis, (E) reprinted under CC BY 4.0 and (F) reprinted with permission from Springer Nature.

3.3.2 Discrete damage models

In discrete damage models the explicit crack topology is introduced as a discontinuity embedded in a continuum. The mechanics inside the crack are also described, i.e. the load transfer between the crack surfaces as a function of crack opening.

Cohesive zone models

Cohesive zone models were developed to model damage in brittle materials (Barenblatt, 1959) and later applied to geomaterials and concrete in order to capture the non-linear processes occurring in front of the crack tip of a propagating crack (De Borst, 2003). In a cohesive zone model, all damage mechanisms in the process zone in front of the crack tip are combined into a cohesive surface. The crack tip separates the stress-free (open) crack from the fracture process zone and the front of the fracture process zone is referred to as the virtual or fictitious crack tip (Fig 3.11A). In this point, the ultimate stress in the crack is equal to the cohesive strength of the intact material σ_c and therefore there is no stress singularity at the crack tip as in the LEFM framework (Khoei, 2014). A constitutive damage evolution law is used to describe the degradation of the cohesive surface. Two simple examples, one linear and one bi-linear model, are illustrated in Figure 3.11B, and they relate the traction t inside the crack to the crack opening δ. The critical crack opening distance is denoted δ_c and t_c is the cohesive strength of the intact material. The area under the traction-separation curve is equal to the fracture energy or critical strain energy release G_c that is needed to completely open the crack.

There are several numerical techniques developed to model cohesive fracture problems, where the two most common ones in bone applications are cohesive elements and the extended finite element method (XFEM) in combination with a cohesive crack description.

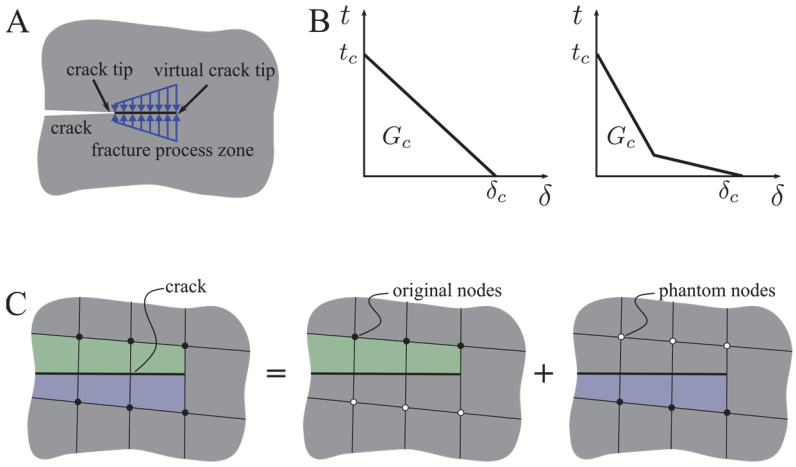

Figure 3.11. (A) Illustration of a cohesive crack. (B) Linear and bilinear traction separation laws used to describe a cohesive crack. (C) Phantom node approach used with XFEM.

Cohesive element models

Cohesive elements are special interface elements that are inserted along the edges of solid elements and this method is therefore also referred to as the inter-element approach (Khoei, 2014). The degradation of the cohesive elements is determined by a traction-separation law and represents the crack opening. Cohesive elements are well suited for applications where the crack path is known a priori, either from experiments or when modelling failure of interfaces or laminated composites, and the cohesive elements can have either a finite or zero thickness (Budhe et al., 2017; De Borst, 2003).

Cohesive elements have been used in various applications to study bone mechanics, e.g. in combination with fracture mechanics tests where inverse methods were used to determine the material parameters (Dourado et al., 2013; Ural and Vashishth, 2006). At the microscale, cohesive elements have been used to simulate crack propagation in microstructural models in 2D to study how the crack path is affected by the microstructure. Mischinski and Ural (2011) simulated crack propagation around an osteon with cohesive elements inserted along two predefined paths, one going through the osteon and one following the cement line around the osteon (Figure 3.10C). A similar approach was used by An and Zhang (2018) to study crack deflection or penetration of a dentin tubule. For more complex geometries where the crack path cannot be predicted beforehand, zero-thickness elements can be inserted in between all solid finite elements. This method has been used to simulate crack paths in cortical bone to evaluate the role of osteons and cement lines (Figure 3.10D-E.) (Mischinski and Ural, 2013; Wang

et al., 2017). However, the method is known to be mesh dependent and all the cohesive surfaces introduce additional compliance in the model (Xu and Needleman, 1994).

Cohesive elements have also been used to model the nano structure of bone. Luo et al. (2011) evaluated how the strength of collagen-mineral interface caused different types of microdamage and suggested that strong interfaces results in the formation of linear microcracks while weaker interfaces cause diffuse microdamage. Similarly, Maghsoudi-Ganjeh et al. (2019) modelled mineralized collagen fibrils embedded in an extrafibrillar matrix and used cohesive elements to describe the interface of non-collagenous proteins separating the two phases and analyzed differences in damage patterns from tensile and compressive loads.

There are only a few examples in literature where cohesive elements have been used to study the fracture process in bone at the organ scale. In whole bone models, the need of prescribed fracture paths is a major disadvantage as substantial knowledge a priori or highly simplified geometries are required. Ural and Mischinski (2013) modelled fracture in an idealized model of the radius by introducing cohesive elements in a crack plane perpendicular to the bone shaft and Mirzaei et al. (2018) instead prescribed complex crack surfaces of subtrochanteric femoral fractures according to their experimental data. Both models were limited to estimate fracture loads.

Extended finite element method

The extended finite element method (XFEM) is a numerical framework using enriched elements with additional degrees of freedom to describe discontinuities (cracks) in the displacement field within solid elements. It was introduced by Belytschko and Black (1999) as a finite element method with minimal remeshing and is based on the concept of partition of unity (Melenk and Babuska, 1996). With this intra-element method, cracks can be arbitrarily oriented and are no longer limited to conform to the edges of the finite elements. The enriched displacement field $\boldsymbol{u}$ is described as

$$\boldsymbol{u}(\boldsymbol{x}, t) = \hat{\boldsymbol{u}}(\boldsymbol{x}, t) + H_{\Gamma_d}(\boldsymbol{x})\tilde{\boldsymbol{u}}(\boldsymbol{x}, t) \tag{7}$$

where $\hat{\boldsymbol{u}}$ and $\tilde{\boldsymbol{u}}$ are continuous functions and H_{Γ_d} a step function describing the discontinuity, often taken as the Heaviside function (Khoei, 2014). The constitutive law describing the discontinuity can be defined in different ways, e.g. using linear elastic fracture mechanics (LEFM) or the cohesive segments approach.

Song et al. (2006) introduced an alternative method to describe the crack by using a superposed element formulation with so called phantom nodes, which are constrained to the original nodes in intact elements. When an element is split by

a crack, it is replaced by two elements (green and blue in Figure 3.11C) that are described by a combination of original nodes and phantom nodes (solid and open circles in Figure 3.11C). The phantom nodes are then released from the original nodes and the separation is described by the cohesive law. The crack topology is implicitly described using level-set theory (Song et al., 2006). This is the methodology that is implemented in Abaqus for the cohesive segments approach (ABAQUS/Standard, 2017), later used in this thesis. In Abaqus, an enriched element can only be intersected by one crack and the crack is required to split an element in two parts so that the crack tip ends along the edge of the split element. Furthermore, new cracks cannot form in a domain if there is already an active crack (ABAQUS/Standard, 2017). For a comprehensive overview of XFEM, readers are referred to (Khoei, 2014).

In XFEM, crack propagation is modelled in two steps: damage initiation and damage evolution. The initiation step describes when, where and in what direction a crack should be introduced. This is modelled with a fracture criterion f and additionally a vector that is perpendicular to the new crack surface needs to be specified. One commonly used fracture criterion for applications in bone mechanics is the maximum principal strain criterion (MAXPE)

$$f_{MAXPE} = \left\{ \frac{\langle \varepsilon_{max} \rangle}{\varepsilon^0_{max}} \right\} \tag{8}$$

where ε_{max} is the maximum principal strain and ε^0_{max} is the critical damage initiation strain. The symbol $\langle\ \rangle$ is the Macaulay bracket which indicates that pure compressive states do not initiate damage. Damage is initiated when $f_{MAXPE} > 1$ and for this criterion the crack is assumed to propagate perpendicular to the principal strain direction. Another criterion, commonly used also for cohesive elements, is the quadratic nominal strain criterion (QUADE)

$$f_{QUADE} = \left\{ \frac{\langle \varepsilon_n \rangle}{\varepsilon^0_n} \right\}^2 + \left\{ \frac{\varepsilon_s}{\varepsilon^0_s} \right\}^2 \tag{9}$$

where ε_n is the normal strain and ε_s is the shear strain. In this case, the crack propagates perpendicular to the normal strain ε_n, i.e. along the surface.

Most XFEM studies on bone have been performed in 2D at the microscale. Budyn and Hoc (2012) were the first to simulate crack propagation in cortical bone with the aim to analyze the effect of the osteonal microstructure (Budyn and Hoc, 2012; Budyn et al., 2008). They used a MAXPE criterion to initialize the crack surfaces and LEFM for the subsequent crack growth law. These models predicted cracks that started from the Haversian canals and continued to grow perpendicular to the

applied load and could not capture crack deflections in the cement lines (Figure 3.10H). In later studies, measured crack paths from experiments were imported into the XFEM models and the deformation in the models were compared to experimental data measured with DIC (Budyn and Hoc, 2010). LEFM models have also been used to study the growth of microcracks in the vicinity of osteons (Najafi et al., 2007; Raeisi Najafi et al., 2009).

The cohesive segments approach, in combination with the MAXPE criterion, has also been used to simulate crack propagation in cortical bone at the microscale (Abdel-Wahab et al., 2012; Idkaidek and Jasiuk, 2017; Idkaidek et al., 2017; Li et al., 2013; Vergani et al., 2014). Like the previous LEFM models, this approach was also unable to capture crack deflections at the osteon boundaries (Figure 3.10I). Recently, Marco et al. (2018a) proposed to use a heterogeneous maximum tangential stress (MTS) criterion where all possible crack paths within a segment in front of the crack tip were evaluated to identify the weakest crack path (Figure 3.10J). This model captures crack deflection in the cement line, however, to obtain crack deflection, some material properties had to be set to values that are quite far from the ranges found in literature (Table 4.1). For example, the stiffness of the cement line was set to be 160 times lower than the matrix stiffness. Rodriguez-Florez et al. (2017) evaluated the effect of intra-cortical porosity in mouse bone using XFEM in Abaqus. They explored the possibility of using multiple enriched subregions to allow for new cracks to form, as cracks cannot initiate in regions where there is an active crack (ABAQUS/Standard, 2017). However, this approach included cumbersome manual work and was not suitable for complex geometries (Rodriguez-Florez et al., 2017).

The problem with using MAXPE to model crack initiation in microstructural models is that cracks nucleate in the Haversian canals (Budyn and Hoc, 2012; Budyn et al., 2008; Idkaidek and Jasiuk, 2017; Idkaidek et al., 2017). This is, however, not observed experimentally, where cracks instead form inside cement lines or within the interstitial matrix (Wolfram et al., 2016). Hence, to capture realistic crack nucleation, local tissue heterogeneity needs to be introduced in the models. Furthermore, for crack nucleation in vivo the fatigue strength is an important factor (Acevedo et al., 2018; Taylor et al., 2007), which is not considered in the current XFEM models.

More realistic predictions of crack initiation have been achieved in applications where porosity was not explicitly modeled, e.g. in the study by Zhang et al. (2016) that used XFEM to model crack initiation in 3D in ceramic dental prostheses using the maximum principal stress (MAXPS) criterion. Furthermore, Feerick et al. (2013) simulated the emergence of cracks during a screw pull-out test in cortical bone in 2D and 3D. In this study, multiple damage criteria were introduced, inspired by Hashin's study of damage for composite failure (Hashin, 1980), to

include the tissue anisotropy. Quadratic nominal stress (QUADS) criteria were used to model crack growth parallel or perpendicular to the osteon directions and the MAXPS criterion was introduced to account for off axis crack predictions (Feerick et al., 2013). Recently, Hammond et al. (2019) used a similar approach to model crack propagation in trabecular bone, exploring the effect of using isotropic or anisotropic tissue with homogeneous or heterogeneous tissue distribution. Here, the QUADS criterion was used to model crack propagation along the trabeculae, specified by the anisotropy, and MAXPS was used for crack propagation in the isotropic models (Hammond et al., 2019). The main limitation in their study was that the two damage criteria were used in separate models, whereby they could not evaluate the competition between the two.

Demirtas et al. (2016) developed a framework including both XFEM and cohesive elements to simulate crack propagation in cortical bone at the microscale in a "quasi-3D" model. Elliptical osteons were outlined in 2D based on microscopy images and then extruded to 3D cylinders running through a block of interstitial matrix material. Crack propagation in osteons and matrix material was modelled with the QUADS criterion and limited to expand in a 2D plane. Cement lines were represented with zero-thickness cohesive elements and crack opening was modelled with a linear traction separation law. Later studies also involved the effects of microcracks inserted in the matrix (Demirtas and Ural, 2018a, b). The main limitation with these models is that the matrix and osteon crack is restricted to grow within the predefined plane and that the crack growth in matrix and cement lines is not connected.

Simulating crack propagation in 3D is much more complicated than the 2D case, especially regarding the description of the crack topology. In 2D, the crack tip is described by a point, while in 3D the crack front is a three-dimensional curve where care needs to be taken so that the crack growth conforms to the crack segments in the neighboring elements (Gasser and Holzapfel, 2006). For bone applications, both model geometries and crack topologies are very complex and numerical convergence is highly challenging. Due to this, the literature considering simulation of crack propagation in bone in full 3D is scarce and models are in general limited to capture crack initiation and a small part of the following crack surface. Ali et al. (2014) used XFEM in Abaqus at the organ scale to simulate the fracture process in five patient-specific femur models using the MAXPE fracture criterion. In this study, the onset of fracture was captured but the complete fracture surfaces could not be predicted due to convergence issues from the 3D cracks expanding in the finite element mesh (Figure 3.10G). A similar case study by Liu et al. (2010), was also limited to predict crack initiation in a proximal femur model in 3D. A slightly different approach was used by Gasser and Holzapfel (2007) to simulate the fracture process in a proximal femur model. They applied a partition

of unity method developed for crack propagation in concrete (Gasser and Holzapfel, 2006), with a cohesive crack description and a non-local (Rankine) stress criterion for crack initiation. The main difference from the other studies was that the crack was smoothed to avoid topological difficulties by fitting the 3D crack surface to a smooth polynomial surface. A simplified homogeneous femur model was used, and the simulations predicted a complete intertrochanteric fracture with a slightly curved crack surface (Figure 3.10F). The study illustrated the benefit of smoothing the 3D crack surface to reduce the numerical problems arising with a complex crack topology in 3D. This type of smooth crack is a reasonable assumption at the organ scale, however, 3D models at the microscale also need to capture crack surfaces containing sharp deflections.

4 Methods

In the first study of this thesis, a multimodal experimental setup was used to measure local deformations at nano- and mesoscale in cortical bone. The tissue microstructure and the crack paths of the tested samples were visualized with high-resolution micro-CT. In the numerical part, a framework for simulating crack propagation in cortical bone was presented. The model was introduced in study II and then further analyzed in a comprehensive material parameter study in study III. In studies IV and V, the framework was applied to realistic cortical bone geometries at the micro- and mesoscale respectively.

4.1 Experimental study (paper I)

Cortical bone samples from the diaphysis of bovine femora oriented parallel and perpendicular to the long axis of the bone were prepared (Figure 4.1A). The samples were spray painted with a random speckle pattern for DIC measurements prior to testing, except for a 1 mm wide strip in the middle of the samples that was left unpainted for SAXS/WAXS measurements (Figure 4.1B). In situ tensile testing was performed under continuous loading (Engqvist et al., 2014) at the I911-4 beamline at MAX II (MAX IV Laboratory, Lund University, Lund, Sweden) (Labrador et al., 2013), with concurrent DIC and SAXS or WAXS measurements (Figure 4.1C). The setup of the DIC system and the SAXS/WAXS acquisition were synchronized such that an image was captured at every instance the x-ray detector acquired data.

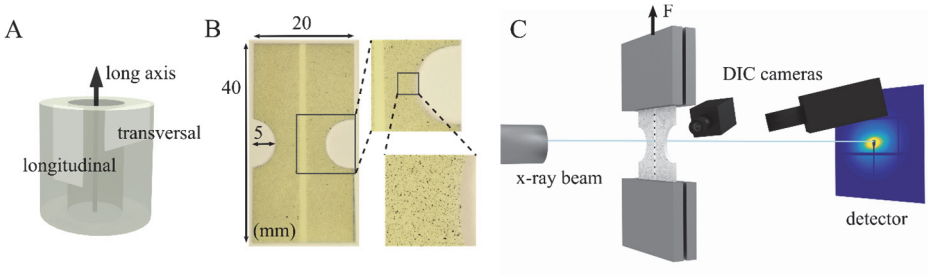

Figure 4.1. (A) Sectioning of bovine cortical bone, where longitudinal samples were cut along the femoral shaft and transversal samples were cut in the perpendicular direction. (B) Symmetric notches were cut out from the samples before they were spray painted with a random speckle pattern. A strip was left unpainted in the middle of the samples for SAXS and WAXS measurements. (C) Experimental setup where in situ loading was applied inside an x-ray beam for SAXS and WAXS measurements and digital cameras were used to record image series for the DIC analysis. Adapted and reprinted from study I with permission from Elsevier.

The digital image correlation of the sample surfaces was performed in 3D using the commercial software Vic-3D 7 (Correlated solutions, Columbia, SC, USA). However, in the WAXS setup, the lighting caused excessive reflections in the images from one of the cameras which made the correlation impossible and 2D-DIC using the images from the one remaining camera was instead performed (Vic-2D 6, Correlated solutions, Columbia, SC, USA). All analyses of SAXS/WAXS data were performed using custom-written scripts in MATLAB (MATLAB version 2014a, The MathWorks, Inc., Natick, Massachusetts) according to (Turunen et al., 2017; Turunen et al., 2014). The collagen fiber orientation was determined from the SAXS scattering pattern, as described in section 3.2.2, and the 3rd order collagen peak was identified by using a Gaussian curve fit to the I(q) curve. The shift of the peak location was used to calculate the collagen strain. From the WAXS scattering pattern, the crystallographic lattice spacing of the mineral phase was determined using Bragg's law (equation 3) and the relative change in lattice spacing during loading compared to the unstressed state was considered as mineral strain (Gupta et al., 2006a).

After mechanical testing, all samples were imaged using high-resolution micro-CT (Zeiss Xradia XRM520, 4D Imaging Lab, Lund University), with an isotropic voxel size of 9.25 µm and a field of view of approximately 18 mm. The micro-CT images were analyzed using ImageJ v1.50i (Schneider et al., 2012) and realigned before the minimum intensity projection was used to visualize the vasculature at the microscale. The orientation of the vascular structure was calculated in each

pixel based on the gradient in a local neighborhood using the plug-in OrientationJ (Püspöki et al., 2016) in ImageJ. The results were visualized using tissue orientation maps showing the angle of orientation in each pixel. The crack paths of the fractured samples were analyzed to quantify the crack length and the irregularity of the crack surface. The crack length was calculated as the Euclidean distance between all boundary pixels in MATLAB (MATLAB version 2015b, The MathWorks, Inc., Natick, Massachusetts), and normalized with 1) the notch width and 2) with the shortest distance between the start and end point of the crack.

4.2 Numerical studies (papers II-V)

To start with, a modelling framework was needed that could be used to analyze the role of microstructure for crack propagation in cortical bone. The following requirements were identified:

a) a model that included microstructural features of cortical bone, e.g. osteons and cement lines
b) a model that could be used to simulate crack paths not known a priori
c) a model that was applicable to different microstructural orientations
d) a model that could capture crack deflections along weak interfaces

As summarized in section 3.3, several modelling strategies are available to simulate crack propagation. In short, the element deletion method was discarded due to its mesh dependency and the cohesive elements due to the need of a predefined crack path. Furthermore, when this project started in 2015, the phase-field method was still immature and had unclear application advantages for our purpose. There were a few studies in literature using XFEM that fulfilled requirements a) and b), e.g. (Abdel-Wahab et al., 2012; Budyn and Hoc, 2012; Li et al., 2013). However, these studies assumed only the MAXPE criterion for crack propagation and could therefore not capture crack deflections in cement lines. Furthermore, they only simulated crack propagation around radial osteons. The idea was therefore to combine XFEM with a criterion for interface damage, inspired by the study by Mischinski and Ural (2011) using cohesive elements and the XFEM study by Feerick et al. (2013) using Hashin damage, and thereby fulfill also requirements c) and d). Damage in cortical bone was assumed to be strain driven, which is in line with e.g. the experimental work by (Nalla et al., 2003). Furthermore, a strain-based modelling framework suits well the experimental techniques for measuring local strain values at different length scales as presented in study I.

4.2.1 The interface damage model

Damage in the cement line was modelled using two different damage criteria to distinguish possible damage mechanisms in the interface: the QUADE criterion for crack propagation along the interface and the MAXPE criterion for crack penetration of the interface. Both criteria were implemented in the user defined damage initiation subroutine UDMGINI in Abaqus Standard (v2017, Dassault Systemes). The criterion for damage initiation was then defined as

$$\max(f_{QUADE}, f_{MAXPE}) > 1 \tag{10}$$

where f_{QUADE} was defined according to equation (9) and f_{MAXPE} according to equation (8). All cement line elements were assigned a normal vector oriented perpendicular to the interface that was used to define the direction of the crack propagation in the QUADE criterion. Crack propagation in matrix, osteon and canal materials was modelled with only the MAXPE criterion, where the crack propagation was assumed to be perpendicular to the principal strain direction. An average normal direction was calculated if the damage criteria changed from MAXPE to QUADE or vice versa, to smoothen the crack path. This approach slightly changed in study V, where instead a maximum deflection angle was introduced to limit how much the crack could turn between two increments. The damage evolution was assumed to be mode independent for all damage criteria and a linear traction-separation law was used to model the degradation of the cohesive crack. The strain energy release rate G was specified as the area under the traction-separation curve.

4.2.2 Model geometries and boundary conditions

The interface damage model has been applied to three types of 2D-models (Figure 4.2). In study II and III, simplified microstructural models were used, where the osteon was assumed to be a cylinder with a diameter of 150 µm and surrounded by a 5 µm thick cement line (Skedros et al., 2005). The osteon was modelled as a rectangle with rounded endpoints in the longitudinal and transversal models and as a circle in the radial model (Figure 4.2A). The normal vectors of the cement line elements were described as material orientations using cylindrical and rectangular coordinate systems in Abaqus CAE (ABAQUS/Standard, 2017).

In study IV, scanning acoustic microscopy (SAM) images were used to create models with more realistic microstructures. In this case, osteons and Haversian canals were segmented manually from the SAM image and fitted with ellipses (Figure 4.2B). The cement line was again assumed to be 5 µm thick. The porosity in the original image was 9% and the size of the Haversian canals was then

increased and decreased to artificially create models with higher and lower porosities. For the elliptic osteons, the normal vectors *n* in all cement line elements were defined in the user defined subroutine ORIENT as the gradient of the ellipse

$$f(x,y) = \frac{x^2}{a^2} + \frac{y^2}{b^2} - 1 = 0 \tag{11}$$

i.e.

$$n = \nabla f = \left(\frac{2x}{a^2}, \frac{2y}{b^2}\right) \tag{12}$$

Finally, in study V, larger mesoscale models based on micro-CT images from the experiments in study I were created by converting tissue orientation maps into XFEM models (Figure 4.2D). Crack growth at the mesoscale was simulated using the interface damage model used in studies II-IV, without resolving the detailed microstructure. The performance of the image-based mesoscale models was verified against microstructural models (Figure 4.2C) including a simplified osteon structure similar to the models in study II and III. In all studies, an initial crack was inserted in each model and crack propagation was simulated under tensile loading (Figure 4.2).

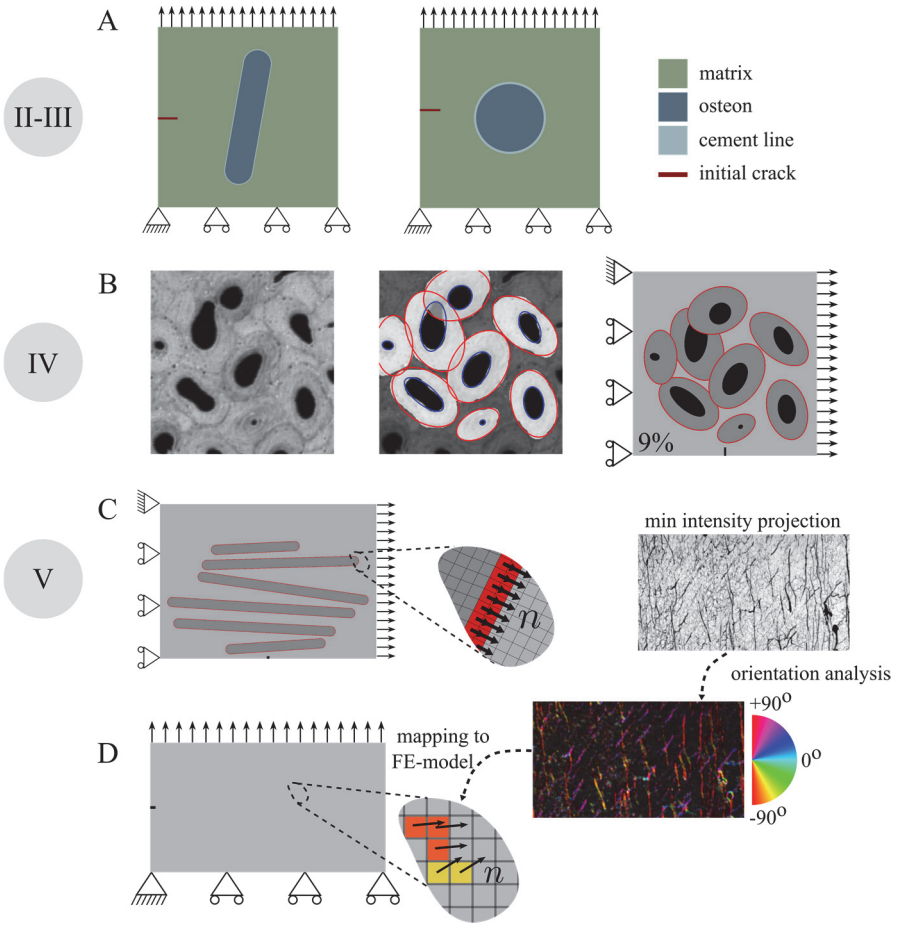

Figure 4.2. Model geometries and boundary conditions. (A) Simplified osteon models used in studies II-III. (B) Models based on a scanning acoustic microscopy image used in study IV. (C) Simplified microstructural osteon models used in study V. (D) Image-based mesoscale models used in study V, where the orientation of the tissue microstructure was mapped from micro-CT images. Adapted and reprinted from studies II-IV with permission from Elsevier.

4.2.3 Material parameters

A literature review was performed to identify material parameter values for cortical bone constituents from both experimental and numerical studies (Table 4.1). Two main things are worth noticing: the scarce experimental damage data for the different cortical bone constituents and the large range of values used for the cement line in numerical studies.

Table 4.1. Material parameters for cortical bone reported in literature. Symbols used in the table: ~ approximate value interpreted from figures; [K] G calculated from a reported stress intensity factor K, where $G=K^2/E$, assuming E=20 GPa (Koester et al., 2008); [T] Transversal osteons (crack parallel to osteons); [L] Longitudinal osteons (crack perpendicular to osteons). Reprinted from study III.

Material parameter	Symbols	Experimental studies	Numerical studies
Young's modulus (GPa)	E_{mat}	13.8-15.3[a]; 10.8[b];	14.122[v,w,x,y]; 14[z]; 14.6[aa,ab,ac]; 14.6-15.4[ad]; 25.8[ae]; 10[af]; 4[ag]; 18.5-27.1[ah]
	E_{ost}	(0.63-0.76)*E_{mat}[c]; 0.91*E_{mat}[d]; ~0.85*E_{mat}[e]; 7.4-18.5[f];	9.13[v,x,z]; 9[z]; 13.5[aa,ab]; 13.5-14.3[ad]; 12.85[w]; 22.5[ae]; 4.4[ag]; 16.6-25.1[ah]; 13.3[ac]
	E_{cl}	$E_{cl} > E_{mat}$[g,h]; $E_{cl} < E_{mat}$[i]; 0.7*E_{mat}[j]	6.85[v,x]; 7[z]; 10.12[aa,ab]; 0.75*E_{ost}[ad]; 9.64[w]; 3.3[ag]; 0.09[ac,ai]
Poisson's ratio	ν_{mat}		0.153[v,w,x]; 0.3[aa,ab,ae,ag]; 0.15[z,af]; 0.24-0.33[ah]
	ν_{ost}		0.17[v,w,x,z]; 0.33[aa,ab]; 0.3[ae,ag]; 0.24-0.33[ah]
	ν_{cl}		0.49[v,w,x,y,z]; 0.41[aa,ab]; 0.3[ag]
Critical damage initiation strain (MAXPE criterion)	$\varepsilon^0_{max,\mathrm{mat}}$	~0.01[k]; 0.005[l,m]; 0.011[n];	0.004[v,x,y,aa,ab,ad]; 0.0065[w]; σ^0_{mat}=0.55*σ^0_{ost}[ac]
	$\varepsilon^0_{max,\mathrm{ost}}$		0.004[v,x,y,aa,ab,ad]; 0.0065[w];
	$\varepsilon^0_{max,\mathrm{cl}}$		0.004[v,x,y,aa,ab,ad]; 0.0065[w]; σ^0_{cl}=0.06*σ^0_{ost}[ac]
Critical interface strain (QUADE criterion)	$\varepsilon^0_{n,\mathrm{cl}}$		$\sigma^0_{n,cl} = \sigma^0_{n,mat}$[ae]
	$\varepsilon^0_{s,\mathrm{cl}}$	$\tau^0_{s,cl}$~0.1*$\tau^0_{s,mat}$[o]; $\tau^0_{s,cl} \lesssim \tau^0_{s,ost}$[p]	$\tau^0_{s,cl}$=0.12*$\tau^0_{s,mat}$[ae]
Strain energy release rate (kJ/m²)	G_{mat}	(~0.6-0.8)[q]; (~0.05[T]-0.2[L])[r]; (~0.05-0.2[K])[s]; (0.05-0.13[K])[k]; ~0.2[t]	0.238[v,w,x,z,ac,af]; 0.09[K,aa]; 0.132[ab]; 0.05[K,ae]; 1.16[ah]
	G_{ost}	($G_{ost} > G_{mat}$)[u]	0.86[v,w,x,z,ac]; 0.11[K,aa];0.120[ab]; 0.05[K,ae]
	G_{cl}		0.146[v,w,x,z]; 0.05[K,aa]; 0.084[ab]; 0.05[K,ae] 0.1629[ac,ag]

[a](Faingold et al., 2014); [b](Nyman et al., 2006); [c](Rho et al., 1999); [d](Rho et al., 2002); [e](Mullins et al., 2009); [f](Hengsberger et al., 2002); [g](Skedros et al., 2005); [h](Milovanovic et al., 2018); [i](Burr et al., 1988); [j](Montalbano and Feng, 2011); [k](Chan et al., 2009); [l](Gargac et al., 2014); [m](Gustafsson et al., 2018); [n](Sun et al., 2010); [o](Dong et al., 2005); [p](Bigley et al., 2006); [q](Norman et al., 1995); [r](Zimmermann et al., 2009); [s](Koester et al., 2008); [t](Nalla et al., 2005); [u](Mullins et al., 2009); [v](Abdel-Wahab et al., 2012); [w](Li et al., 2013); [x](Vergani et al., 2014); [y](Budyn and Hoc, 2012); [z](Baptista et al., 2016); [aa](Idkaidek and Jasiuk, 2017); [ab](Wang et al., 2017); [ac](Idkaidek and Jasiuk,

2017); [ad](Budyn et al., 2008); [ae](Demirtas et al., 2016); [af](Rodriguez-Florez et al., 2017); [ag](Giner et al., 2017); [ah](Mischinski and Ural, 2011); [ai](Nobakhti et al., 2014)

In studies II-V, linear isotropic elasticity was assumed for all constituents in the microstructural cortical bone models, with material parameters according to Table 4.2. The hyper-mineralized cement lines were assumed to be 20% stiffer and osteons were assumed to be 20% less stiff than the matrix. The damage initiation strain ε_{max}^{0} for the MAXPE criterion and the strain energy release rate G were both assumed to be equal for all constituents, as separate values cannot be distinguished experimentally. The strain energy release rate of the Haversian canals was scaled to its Young's modulus to have approximately the same ratio between E and G as the other constituents (Rodriguez-Florez et al., 2017). As experimental data regarding critical strains for interface damage was lacking, threshold values for crack penetration and crack deflection in osteon models with and without Haversian canals were identified in study II. For this case, the normal and shear strengths of the interface were assumed to be equal, i.e. $\varepsilon_{n,cl}^{0} = \varepsilon_{s,cl}^{0}$. Moreover, in study II, crack propagation was also simulated assuming that the MAXPE criterion alone could be used to predict crack paths in cortical bone, as had been proposed in previous studies, e.g. (Abdel-Wahab et al., 2012; Li et al., 2013).

Table 4.2. Material parameters. Young's modulus, Poisson's ratio, critical damage initiation strain for the MAXPE criterion and the strain energy release rate specified for interstitial matrix, osteons, Haversian canals and cement lines.

	interstitial matrix	**osteon**	**Haversian canal**	**cement line**
E (GPa)	15[a]	12[b]	0.1	18[c]
ν	0.3	0.3	0.3	0.3
$\boldsymbol{\varepsilon_{max}^{0}}$	0.004[d]	0.004[d]	0.004[d]	0.004[d]
G (kJ/m²)	0.2[e]	0.2[e]	0.001	0.2[e]

[a](Faingold et al., 2014; Hengsberger et al., 2002), [b](Rho et al., 1999, 2002), [c](Skedros et al., 2005), [d](Abdel-Wahab et al., 2012; Budyn et al., 2012; Gustafsson et al., 2018), [e](Koester et al., 2008; Nalla et al., 2006)

Material parameter ranges in study III

In study III, a comprehensive material parameter study was performed in three steps (Figure 4.3) based on the Design of Experiments approach using fractional factorial designs to identify important parameters (factors) in the damage interface model.

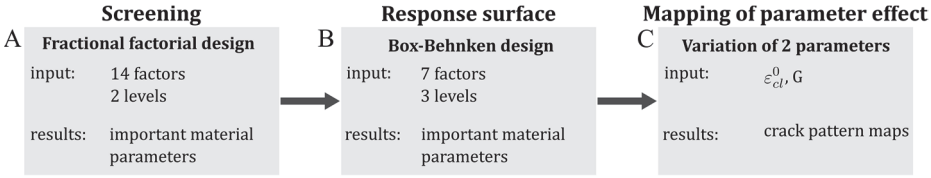

Figure 4.3. Overview of material parameter study performed in study III, including (A) a screening study, (B) a response surface and (C) mapping of parameter effect.

The parameter set used in study II (Table 4.2) was used as baseline values and the average value between crack penetration and deflection identified in study II was used as baseline value for the critical strains for interface damage. Each factor was assigned a parameter space that was ± 20% of the corresponding baseline value (Table 4.3).

Table 4.3. Material parameters used in the screening experiment with two levels (low and high) and 14 factors (X_{screen}) and the Box-Behnken surface design with three levels (low, baseline and high) and 7 factors (X_{BB}). Subscripts "mat", "ost" and "cl" refer to matrix, osteon and cement line respectively and superscripts L, R and T refer to longitudinal, radial and transversal models respectively.

material parameter	factor levels			X_{screen}	X_{BB}
	low (-20%)	baseline	high (+20%)		
E_{mat} (GPa)	12	15	18	1	-
E_{ost} (GPa)	9.6	12	14.4	2	1
E_{cl} (GPa)	14.4	18	21.6	3	2
ν_{mat}	0.24	0.3	0.36	4	-
ν_{ost}	0.24	0.3	0.36	5	-
ν_{cl}	0.24	0.3	0.36	6	-
$\varepsilon_{max,mat}^{0}$	0.0032	0.004	0.0048	7	-
$\varepsilon_{max,ost}^{0}$	0.0032	0.004	0.0048	8	-
$\varepsilon_{max,cl}^{0}$	0.0032	0.004	0.0048	9	3
$\varepsilon_{n,cl}^{0}$	0.00084^{L} 0.0012^{R} 0.0028^{T}	0.00105^{L} 0.0015^{R} 0.0035^{T}	0.00126^{L} 0.0018^{R} 0.0042^{T}	10	4
$\varepsilon_{s,cl}^{0}$	0.00084^{L} 0.0012^{R} 0.0028^{T}	0.00105^{L} 0.0015^{R} 0.0035^{T}	0.00126^{L} 0.0018^{R} 0.0042^{T}	11	4
G_{mat} (kJ/m^2)	0.16	0.2	0.24	12	5
G_{ost} (kJ/m^2)	0.16	0.2	0.24	13	6
G_{cl} (kJ/m^2)	0.16	0.2	0.24	14	7

In the screening and response surface designs (Figure 4.3A-B), analysis of variance (ANOVA) was used to identify the most important factors for different outcome parameters under the assumption that important factors give a large contribution to the variance. The evaluated outcome parameters were the maximum force (peak value in load curve), fracture energy (area under load curve), crack length (from the coordinates of all crack segments) and crack score. The crack scores were used to categorize the crack pattern (Figure 4.4).

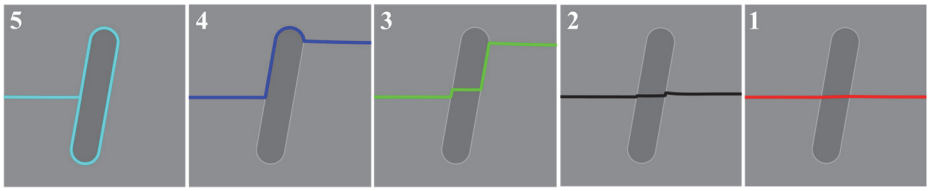

Figure 4.4. Crack scores used to categorize the crack pattern ranging from 1 to 5.

The analysis followed the work by (Isaksson et al., 2008), where the percentage of the total sum of squares for each factor (%TSS) represented the contribution of each factor to the variance and was considered a measure of the importance of each factor. First, a two-level screening experiment (Figure 4.3A) was carried out, where the main effects were assumed to be clear of two-factor interactions (Montgomery, 2005). The design contained 14 factors ($\mathbf{X}_{screen}$ in Table 4.3) and 32 treatment conditions (simulations with different combination of factors). Next, a subset of the most important factors was further analyzed using a response surface design (Figure 4.3B). A Box-Behnken design was used with 7 factors ($\mathbf{X}_{BB}$ in Table 4.3), three levels and 62 treatment conditions. The three levels were created by adding the baseline value as a middle value between the low and high levels (Table 4.3). The critical interface normal and shear strains were in this case assumed to be equal. Both designs were generated with the software JMP. The final part of the parameter study consisted of mapping the effect of fracture energy G and critical interface strains ε_{cl}^{0} over a wider range of values, while keeping the other parameters constant (Figure 4.3C).

The effect of age-related properties

Possible underlying mechanisms for the altered crack pattern and fracture behavior of old bone were analyzed in study IV. The effects of porosity and fracture energy were compared using models based on microscopy images of cortical bone (Figure 4.2B-C). Crack propagation was simulated in models with porosities ranging from 0-15%, as these values span over the average cortical porosity reported in literature (e.g., 4% - 9% in femoral shaft of women between 20 and 100 years with no

known bone diseases (Feik et al., 1997), 8% - 16% in femoral shaft of men between 20 and 80 years with no known bone diseases (Malo et al., 2013)). Similarly, the fracture energy was varied between 0.05 and 0.4 kJ/m^2, which corresponds to the range of reported damage initiation toughness for young and old bone (Chan et al., 2009; Koester et al., 2008; Nalla et al., 2005; Norman et al., 1995; Zimmermann et al., 2009). For all cases, the remaining parameters were defined according to Table 4.2.

Parameters for mesoscale models

For the image-based mesoscale models (Figure 4.2D) in study V, the cortical bone tissue was assumed to consist of isotropic matrix material according to Table 4.2, except for the fracture energy G that was assumed to be 0.4 kJ/m^2 (instead of 0.2 kJ/m^2) as this facilitated the numerical convergence. The baseline values for the critical interface normal and shear strains were both assumed to be 0.0015, and the effect of weaker interfaces was evaluated. For the microstructural models (Figure 4.2C) in study V, the material parameters for matrix, osteon and cement line were defined according to Table 4.2, except for the fracture energy G that was assumed to be 0.4 kJ/m^2.

5 Results

5.1 Experimental study

The microstructure of the samples was assessed from the micro-CT images (Figure 5.1A-C). In the transversal (Figure 5.1A) and longitudinal (Figure 5.1B) samples, the main fiber orientation was clear, with parallel fibers throughout the samples. The heterogeneous sample (Figure 5.1C) displayed two different tissue types with different micro-orientations: Haversian tissue with longitudinal osteons in the lower left part and lamellar tissue with oblique orientation in the right part. The fracture paths followed the fiber orientations in both the transversal and the heterogeneous samples, resulting in smooth and straight crack surfaces (Figure 5.1D, F). The longitudinal sample had a more irregular crack path (Figure 5.1E) and a higher maximum force compared to the other samples (Table 5.1).

Table 5.1. Maximum force and normalized crack lengths for samples with different microstructural orientations. Reprinted from study I with permission from Elsevier.

Microstructural orientation	**F_{max} (N)**	**Crack length normalized with notch width**	**Crack length normalized with shortest crack distance**
Transversal	269	1.095	1.083
Longitudinal	414	1.193	1.166
Heterogeneous	318	1.479	1.111

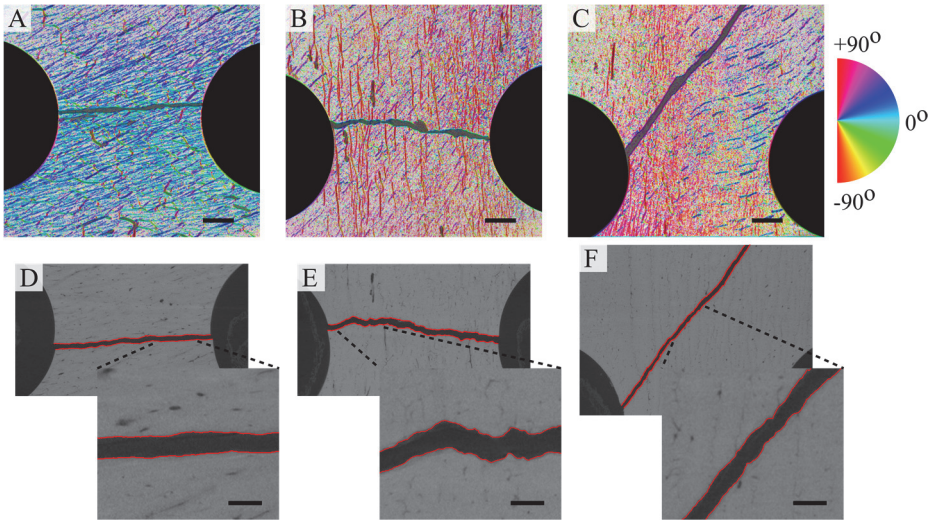

Figure 5.1. (A) Angular distribution of tissue microstructure in (A) transversal, (B) longitudinal and (C) heterogeneous samples. (D-F) The corresponding crack paths used to calculate the normalized crack lengths. Scale bars in (A-C) are 2 mm and scale bars in (D-F) are 500 µm. Adapted and reprinted from study I with permission from Elsevier.

The local deformations on the sample surfaces were analyzed with DIC. There was a problem with samples slipping in the grips, and therefore not all samples fractured. In the samples that fractured, the location of maximum strain in the notch coincided with the crack initiation point (Figure 5.2A-B). There was an asymmetric strain distribution concentrated in the lower part of the left notch in the heterogeneous sample, which coincided with the region of Haversian bone tissue (Figure 5.2B). For this sample, the crack initiated in the region with high strain in the notch and then followed the microstructure visualized in Figure 5.1C. The local tissue strain value at the fracture point was around 0.5% in all samples that were loaded until failure.

Strains at the nanoscale were measured with SAXS and WAXS. The orientation of the microstructure had a large influence on the strains in both collagen fibers and mineral crystals, where higher strains were found in longitudinal samples, i.e. samples loaded along the fiber directions (see Figure 5.2C-D for examples of collagen and mineral strains as a function of load step). In longitudinal samples, strains in the collagen fibers reached a plateau around 0.2% strain while the strains in the mineral crystals increased linearly up to a maximum value around 0.1%. In the heterogeneous sample, higher mineral strains were found in regions where the

microstructure was oriented parallel to the load direction, compared to regions where the microstructure had an oblique orientation (Figure 5.2D).

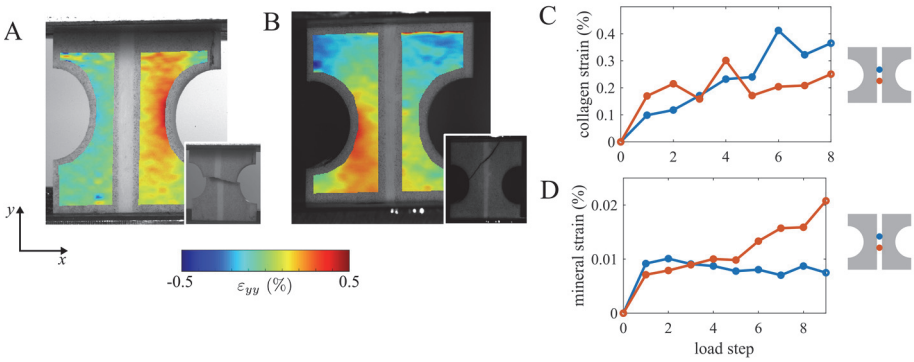

Figure 5.2. (A) Surface strains at the mesoscale measured with 3D-DIC in the load step before fracture. High strain concentrations are only seen in the right notch, due to slippage in the left grips. (B) Surface strains in the heterogeneous sample before fracture measured with 2D-DIC. (C) Typical collagen strains in a longitudinal sample measured with SAXS. (D) Strains in mineral crystals in the heterogeneous sample. In (C) and (D), average nanoscale strains are plotted in two regions inside the notch (blue and orange points). Adapted and reprinted from study I with permission from Elsevier.

5.2 Numerical studies

5.2.1 Model development

Crack propagation around an osteon was first simulated using only the MAXPE criterion. However, as shown in Figure 5.3, the MAXPE criterion always predicted crack propagation through the osteons, i.e. the cement line interfaces did not deflect the cracks. In models containing a Haversian canal, crack deflections were predicted inside the soft canal (Figure 5.3B). This simple example illustrated that an additional interface damage criterion was needed to capture crack deflection in the cement line, as the small mismatch in stiffness between the cement line and the surrounding tissue did not alter the principal strain directions (blow-up in Figure 5.3A). However, inside the canal, where the stiffness was more than 100 times lower than in the surrounding tissue, the principal strain directions did change (blow-up in Figure 5.3B), and the crack was reoriented.

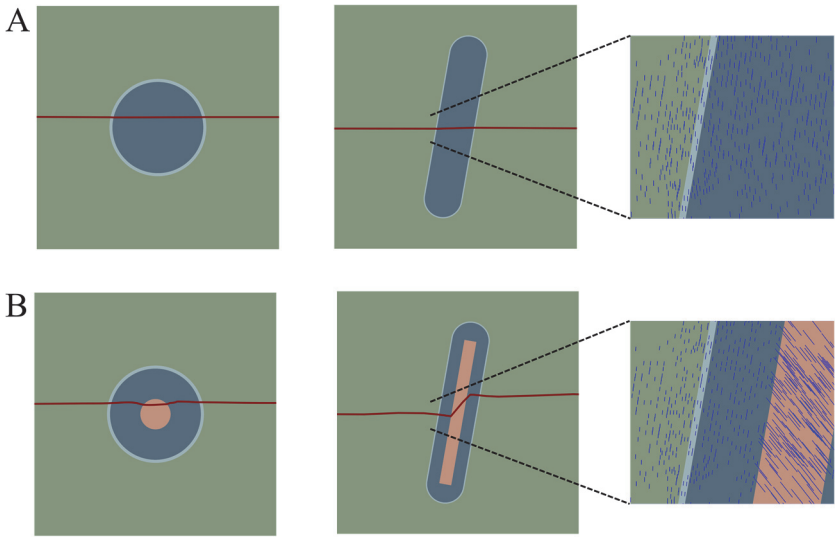

Figure 5.3. Crack propagation simulated with only the MAXPE criterion in models (A) without Haversian canals and (B) with Haversian canals. The maximum principal strain directions are visualized in blue for the longitudinal models where reorientation of the strain field can be seen inside the Haversian canal in (B). Adapted and reprinted from study II with permission from Elsevier.

Additional simulations were performed using only the MAXPE criterion, and variations in the predicted crack patterns were found when comparing models solved with Abaqus standard v6.12, v6.14, v2016 and v2017 (Figure 5.4). Early Abaqus versions (v6.12 and v6.14) seemed to be more sensitive to irregularities in the mesh and two typical examples are marked with white dashed lines in Figure 5.4E-G. When using v6.12, two sharp crack deflections were found inside the osteon material, caused by the mesh irregularities (Figure 5.4E). In that same region, but using v6.14 to solve the problem, the crack instead stopped and simulations failed to converge (Figure 5.4F). This problem was not seen when using newer versions of the software (v2016 and v2017).

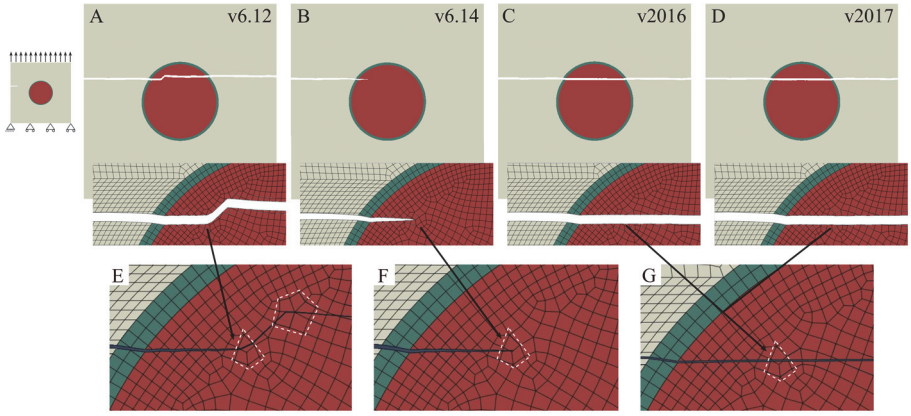

Figure 5.4. Crack propagation simulated with the MAXPE criterion with different versions of Abaqus standard: (A) version 6.12, (B) version 6.14, (C) version 2016 and (D) version 2017. (E) Sharp crack deflections predicted in regions with irregular mesh (marked in white) with version 6.12. (F) The crack stopped in this region in version 6.14 and the simulation failed to converge. (G) Recent versions (v2016 and v2017) were less affected by mesh distortions and a smooth crack path was predicted through the region that was problematic in earlier Abaqus versions.

A mesh sensitivity analysis was performed in several steps in study II. A tensile test of a 1x1 mm^2 homogeneous matrix model comparing both elements with full and reduced integration (CPS4 vs CPS4R) showed that both the maximum force (Figure 5.5A) and the fracture work calculated as the area under the force-displacement curve (Figure 5.5B) converged when using quadratic elements with sides of 10 µm or less. For refined meshes, no difference was seen between elements with full or reduced integration. Equal crack paths were also predicted when simulating crack propagation in microstructural models using elements with full and reduced integration (Figure 5.5C). Finally, different mesh densities inside the cement line interface (1,2,3 or 4 elements across the interface) were evaluated (Figure 5.5D). No notable differences were found when comparing the results for the different mesh densities inside the cement line. In all following microstructural models (studies II-V), the maximum element size was 10 µm and the cement line interfaces were always meshed with at least two elements across the interface thickness.

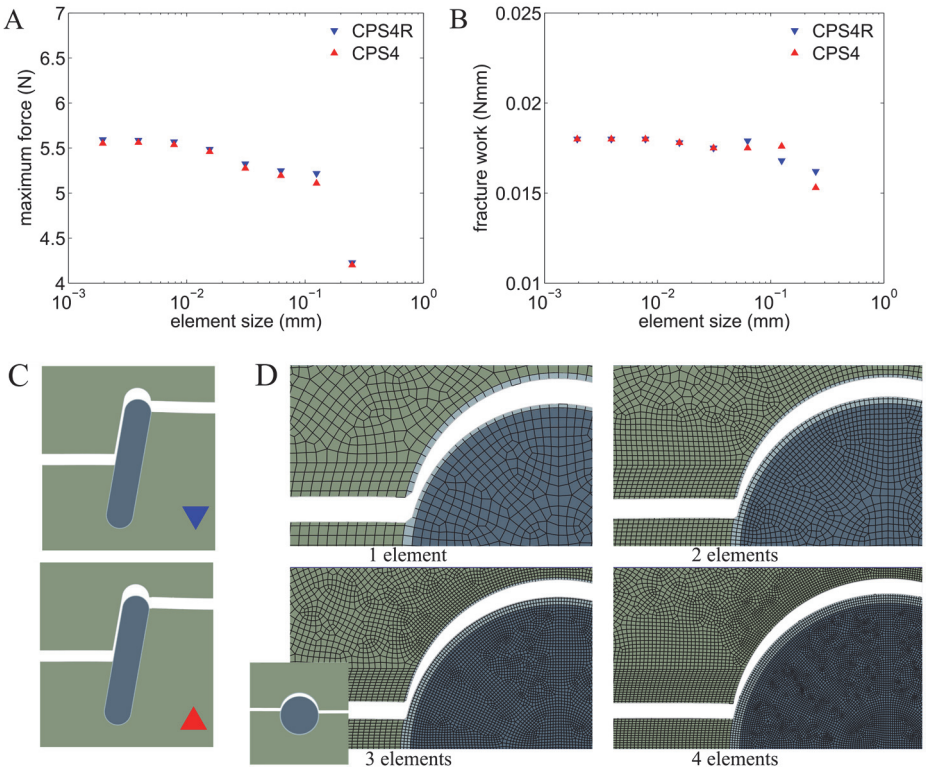

Figure 5.5. Mesh sensitivity analysis where (A) maximum force and (B) fracture work were used as convergence indicators in a tensile test of a 1x1 mm^2 homogeneous matrix model. Elements with full (CPS4 in red) and reduced (CPS4R in blue) integration were analyzed and the crack paths are illustrated in (C). (D) Crack paths for different mesh densities in the cement line. Adapted and reprinted from supplementary material of study II with permission from Elsevier.

Critical interface strains for crack penetration and crack deflections in osteon models without Haversian canals are presented together with typical crack paths in Figure 5.6. These results were used to define the baseline values for the interface strengths in study III.

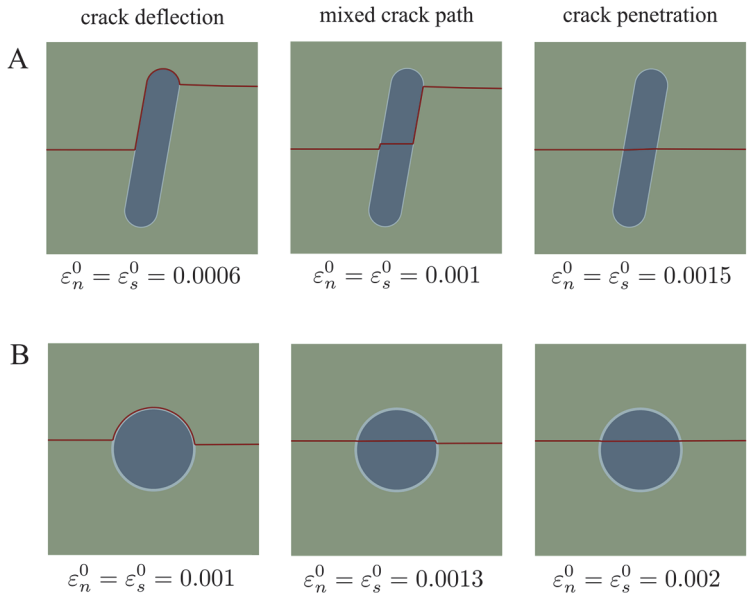

Figure 5.6. Critical interface strains for crack penetration and crack deflections in osteon models without Haversian canals with (A) a longitudinal osteon and (B) a radial osteon. Adapted and reprinted from study II with permission from Elsevier.

5.2.2 Identification of important material parameters

ANOVA was used to identify the most important factors for four outcome criteria (maximum force, fracture energy, crack length and crack score). In the screening design, seven factors were identified as important (E_{ost}, E_{cl}, $\varepsilon^0_{max,cl}$, $\varepsilon^0_{s,cl}$, G_{mat}, G_{ost} and G_{cl}). The fracture energy outcome was dominated by the strain energy release rate G of the different materials. The crack length and crack score outcomes showed similar results, where E_{cl}, $\varepsilon^0_{max,cl}$, $\varepsilon^0_{s,cl}$ and $\varepsilon^0_{n,cl}$ were important factors ($\varepsilon^0_{s,cl}$ scored highest for longitudinal and radial models, whereas $\varepsilon^0_{n,cl}$ was most important for the transversal model).

The result of the Box-Behnken surface design experiment confirmed the results from the screening design. The prediction profiles showed non-linear behavior for factors associated with the cement line (Figure 5.7). Most obvious was the effect of the cement line on the crack length, where high damage initiation strain (MAXPE criterion) and low critical interface strains (QUADE criterion) promoted crack deflection. The material toughness parameters showed modest effects at the evaluated levels. The interactions scored low in general and significant interactions involved factors that were already identified as important.

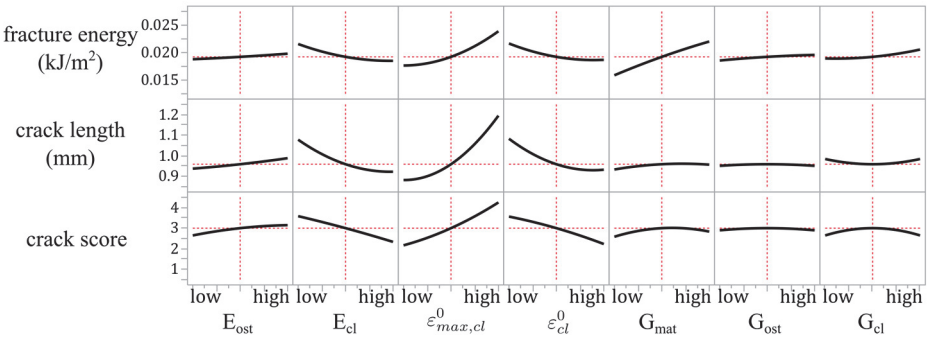

Figure 5.7. Prediction profiles for the longitudinal model from the Box-Behnken analysis. Reprinted from study III with permission from Elsevier.

Both the material toughness and the critical interface strains affected the crack trajectory (Figure 5.8). In general, low material toughness and high interface strength promoted crack penetration of the osteon, while high toughness and low interface strength promoted crack deflection in the cement line. Asymptotic trends were reached for high toughness values (G>0.2 kJ/m^2) for all osteon orientations.

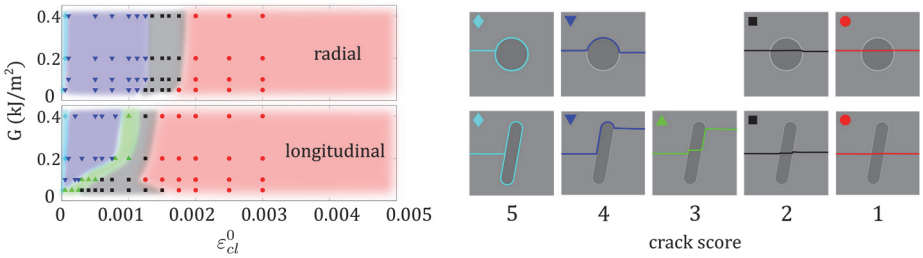

Figure 5.8. Crack score as a function of the strain energy release rate ($G=G_{mat}=G_{ost}=G_{cl}$) and the critical interface strains ($\varepsilon^0_{cl}=\varepsilon^0_{n,cl}=\varepsilon^0_{s,cl}$). Each point in the graph corresponds to a simulation and colored regions are drawn to visualize the region of each crack score. Results are shown for radial and longitudinal models. Adapted and reprinted from study III with permission from Elsevier.

5.2.3 Effect of porosity and tissue integrity

The microstructure in cortical bone clearly affected the crack trajectory through two competing mechanisms: crack deflection in cement lines and crack attraction from Haversian canals (Figure 5.9). Crack paths were longest in models with intermediate porosity levels, as both mechanisms had a positive influence on the

length of the crack path (Figure 5.9B). At low porosity, the crack still deflected in the cement line interface, however, the pores did not attract the cracks and the resulting crack path was shorter (compare Figure 5.9A and B). At high porosities, the crack penetrated the cement lines and propagated through the osteons and Haversian canals (Figure 5.9C). The porosity levels were also reflected in the force-displacement curves (Figure 5.9D), where increased porosity rendered lower structural stiffness as well as lowered peak force along with an increased ability to absorb energy before failure. Porous models displayed a ductile response, followed by a sudden drop in load bearing capacity. The fracture energy could also be related to crack length, where low fracture energy resulted in straighter and shorter cracks that propagated through the microstructure (Figure 5.9E-G). The effect was also clearly visible in the force-displacement curve (Figure 5.9H), where models with low fracture energy displayed a brittle behavior and models with high fracture energy showed a ductile response.

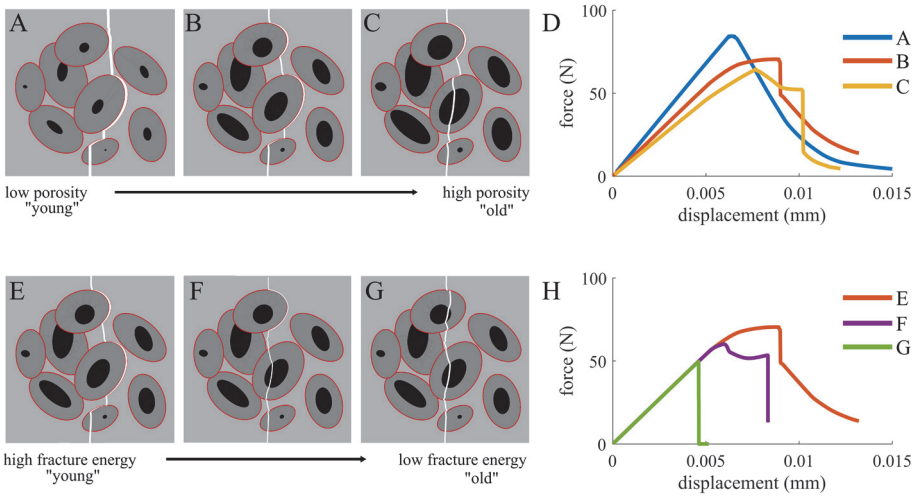

Figure 5.9. (A-D) Influence of porosity on the mechanical response. Models with (A) 2%, (B) 9% (C) 15% porosity were evaluated. (D) Force-displacement curves corresponding to the microstructures in (A)-(C). (E-H) Influence of fracture energy on the mechanical response in models with 9% porosity. The fracture energies (E) 0.4 kJ/m^2, (F) 0.1 kJ/m^2 and (G) 0.05 kJ/m^2 were evaluated. (H) Force-displacement curves corresponding to the microstructures in (E)-(G). Adapted and reprinted from study IV with permission from Elsevier.

5.2.4 Effect of tissue orientation

Microstructural and image-based mesoscale models predicted similar crack paths and mechanical behavior for all simplified osteon models (Figure 5.10), and the mesh density in the mesoscale models did not notably affect the results. Crack propagation through osteons was predicted for baseline parameters when the osteons were oriented perpendicular to the growing crack (Figure 5.10A). For a weaker cement line interface (ε_{cl}^{0}=0.0004), a major crack deflection was observed along the third osteon, and in this case, the microstructural model predicted one sharp turn, while the image-based mesoscale models contained several minor deflections (Figure 5.10B).

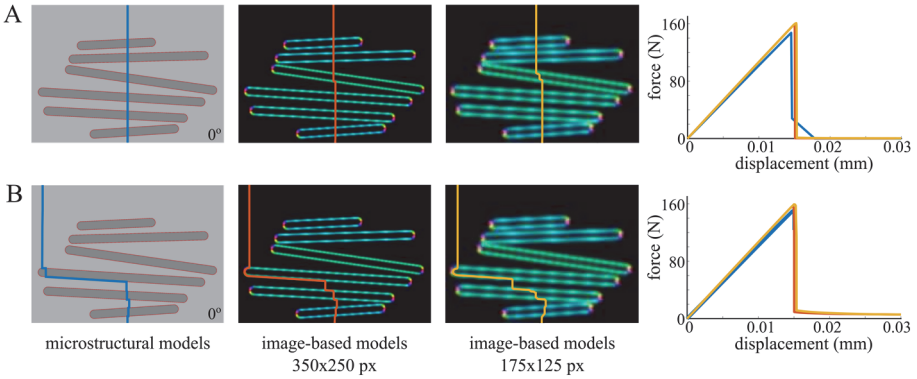

Figure 5.10. Crack patterns and force-displacement curves for three different models: microstructural model (blue line), mesoscale model with 10 µm elements (orange line) and mesoscale model with 20 µm elements (yellow line). Crack propagation simulated in 0° osteon models with (A) baseline parameters and (B) weak interfaces (ε_{cl}^{0}=0.0004).

The predicted crack paths in the micro-CT based mesoscale models are visualized in Figure 5.11. In the transversal models, the cracks closely followed the tissue orientation (Figure 5.11A), while the cracks were more irregular in the longitudinal models (Figure 5.11B). In this case, the crack patterns were characterized by straight horizontal segments alternated with shorter sharp deflections along the interfaces appearing throughout the path. Weaker interfaces in the longitudinal models resulted in more irregular crack paths with larger crack deflections (Figure 5.11C). This also resulted in a higher maximum force compared to the baseline models (Table 5.2). Weaker interfaces in the transversal models did not affect the results.

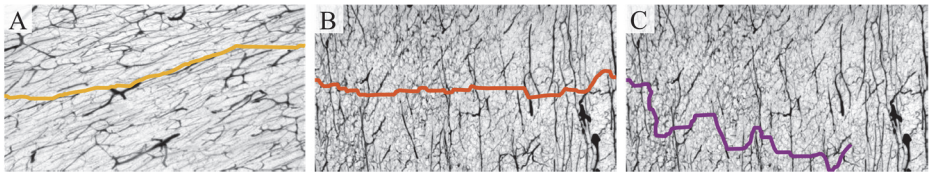

Figure 5.11. Simulated crack paths in the (A) transversal and (B) longitudinal models. (C) Weaker interfaces (ε_{cl}^{0} = 0.0012) resulted in longer and more irregular crack paths in the longitudinal model.

Table 5.2. Average results simulated with image-based mesoscale models in study V and experimental results from study I.

Method	Tissue orientation	F_{max} (N)	Crack length normalized with sample (notch) width	Crack length normalized with shortest crack distance
Image-based mesoscale models	**transversal**	553	1.0560	1.031
	longitudinal	600	1.087	1.092
	longitudinal (weak interface)	673	1.953*	1.671
Experimental results	**transversal**	269	1.095	1.083
	longitudinal	414	1.193	1.166

* normalized with maximum crack length in x-direction (end point of the crack in Figure 5.11C)

6 Discussion

The overall aim of this thesis was to analyze the role of the microstructure for crack propagation in cortical bone using both experimental and numerical techniques. The multimodal experimental analysis in study I linked local deformations measured at nano- and mesoscale to the tissue microstructure. Furthermore, the analysis of the crack pattern underlined the link between the local microstructure and the crack trajectory through the tissue. The crack growth was in turn studied in detail using the XFEM framework for simulating crack propagation and an interface damage model was proposed to describe how cracks are deflected by weak interfaces at the microscale. During the thesis work, various geometrical representations of cortical bone were evaluated, starting from a simplified 2D representation of one osteon in study II and III. The complexity of the model geometries increased in study IV and multiple osteonal structures and Haversian canals based on microscopy images were included. In the last study (study V), instead of resolving the structural features of osteons and cement lines, the microstructure was simplified and represented by the tissue vasculature in micro-CT based mesoscale models. The main findings and limitations of the work are discussed in the following sections.

6.1 Linking multi-scale deformations to micro-structure

In study I, a multimodal experimental setup originally developed for polymers (Engqvist et al., 2014) was adopted to measure deformation at macro-, meso- and nanoscale concurrently in bovine cortical bone using in situ testing in combination with DIC and SAXS/WAXS. The results underlined the importance of the microstructural orientation at different length scales. At the tissue scale, higher peak forces were measured in longitudinal compared to transversal samples (Table

5.1). At the mesoscale, the microstructure was shown to affect the irregularity of the crack path. At the nanoscale, higher strains were found in both collagen fibers and mineral crystals when oriented parallel to the direction of the tensile loading. The local tissue strain measured with DIC in the load step before fracture was approximately 0.5% in both transversal, longitudinal and heterogeneous samples. However, the current DIC setup did not capture the fracture event as the collection of digital images was synced with the SAXS/WAXS measurements and therefore limited to approximately 2 images per minute.

An important lesson from study I was the understanding and solving of the challenges with sample preparation of bovine cortical bone. Sectioning longitudinal and transversal specimens relative to the femoral shaft, as indicated in Figure 4.1, is a standard procedure. The micro-CT images revealed large variations in tissue orientation and structure, which highlights the fact that global landmarks, such as the longitudinal axis of the shaft, are insufficient for preparing samples for micromechanical testing. Based on the micro-CT images, a few samples sectioned in the longitudinal orientation were found to be cut at a slight angle and therefore re-characterized as radial samples (microstructure oriented in the out-of-plane direction). Furthermore, bovine cortical bone contains both Haversian and lamellar/plexiform microstructure (Mayya et al., 2016), and both tissue types were identified among the tested samples.

Study I also highlighted the importance of using local measurement techniques in samples with large spatial variations. The heterogeneous sample showed several examples of this:

- The microstructural orientation evaluated with micro-CT after the test explained the oblique crack path (Figure 5.1C).
- The unsymmetrical strain distribution with high strains below the left notch (Figure 5.2B) could be mapped to regions with Haversian bone (red region in Figure 5.1C), and Haversian bone has lower stiffness compared to the lamellar/plexiform bone (Lipson and Katz, 1984).
- The magnitude of the mineral strains followed the main orientation of the microstructure (Figure 5.2D). Higher mineral strains were found in the lower half of the sample where the tissue orientation was oriented along the tensile load, compared to the mineral strains in the upper half of the sample where the microstructure had an oblique orientation.

6.2 An interface damage model for cortical bone

The take home message from study I was that deformation and damage at both nano- and mesoscale were closely linked to the bone architecture at the microscale. This idea is not new and the importance of the osteons for crack propagation has been the topic in many experimental studies, e.g. (Chan et al., 2009; Koester et al., 2008; Koester et al., 2011; Mohsin et al., 2006; O'Brien et al., 2007). Computational models for simulating realistic crack growth in cortical bone were, however, missing in the literature and the remaining part of this thesis work focused on developing a numerical framework for crack propagation centered around the role of the osteonal microstructure.

The interface damage model was introduced in study II and the key feature of the XFEM model was the use of an additional interface damage criterion based on the normal and shear strength of the interface. The capability of capturing crack deflections in the cement line was demonstrated for different osteon geometries (Figure 5.6). For comparison, crack propagation was simulated with only the MAXPE criterion, assuming that crack deflections were caused by a mismatch in local stiffness between matrix and cement lines. The results in Figure 5.3 showed that this was not a valid assumption, as the models always predicted crack penetration of the interface and a 20% mismatch in stiffness did not notably reorient the strain field in the interface. For large local differences in stiffness, e.g. from introducing a Haversian canal with more than 100 times lower stiffness than the surrounding tissue, the strain field reoriented inside the canal (Figure 5.3). Mechanisms through which interfaces and pore spaces can influence crack growth in cortical bone were studied more in detail in study IV. Two competing mechanisms were identified: Haversian canals attracted the crack by altering the surrounding strain field and caused smooth and meandering crack patterns, while cement line interfaces deflected the cracks causing sharp turns in the crack path (Figure 5.9).

The material parameter study (study III) was motivated by the fact that local material parameters characterizing cortical bone are not well-determined experimentally (Table 4.1). The lack of local parameters has several consequences for the input parameters used in computational models. One effect is that *one* set of damage parameters (the parameters used in (Abdel-Wahab et al., 2012)) has been used extensively in studies simulating crack propagation in cortical bone (e.g. (Baptista et al., 2016; Li et al., 2013; Vergani et al., 2014; Wang et al., 2017)), even though these parameters were originally based on loose assumptions. Furthermore, the values used for the cement line stiffness vary with more than two orders of magnitude in computational studies (Table 4.1). The importance of material parameters for simulating crack propagation in cortical bone was

addressed using ANOVA in a comprehensive material parameter analysis in study III. Experimental techniques for characterizing damage parameters in cortical bone are limited to measuring average values at the mesoscale. Therefore, equal baseline values for ε_{max}^{0} and G were used for both matrix, osteons and cement lines to see the effect of perturbations around the average values. The baseline values for the critical interface strains were instead based on the simulations in study II, as no experimental data was available in the literature. All factors were varied ±20% around the baseline values to give them the same relative importance. The assigned parameter space predicted a wide range of crack patterns. In general, the cement line properties were identified to be important for the capability of deflecting cracks. This was expected and agreed with a previous study using cohesive elements (Mischinski and Ural, 2011). Additionally, the interplay between the interface properties and the cohesive state inside the crack when encountering an interface was analyzed. Low fracture energy ($G \leq 0.2$ kJ/m^2) was found to affect the crack trajectory, while asymptotic trends were reached for high toughness values ($G > 0.2$ kJ/m^2) for all osteon orientations (Figure 5.8). This aspect was not evaluated by the studies using cohesive elements, where Mischinski and Ural (2011) kept the fracture toughness in the matrix fixed at high values (fracture toughness for normal mode was G_n=1.16 kJ/m^2 and shear mode G_s=2.97 kJ/m^2) and Parmigiani and Thouless (2006) modelled a fully open crack impinging on an interface. For the simplified geometries used in study III, the matrix toughness had a large influence for values between 0.05 and 0.2 kJ/m^2, which span the range of values for damage initiation reported for old and young bone (Chan et al., 2009; Koester et al., 2008; Nalla et al., 2005; Norman et al., 1995; Zimmermann et al., 2009). The results from study III could help explain the altered crack patterns seen in old bone, and study IV was devoted to analyzing this aspect in more detail using realistic model geometries based on microscopy images of cortical bone.

The increasing fracture risk with age is believed to be related to both structural and compositional changes in the tissue (Burr, 2019). In study IV, increased porosity represented a typical structural change in old bone and decreased fracture toughness was used to model impaired material integrity related to alterations in the collagen phase (Unal et al., 2018; Willett et al., 2019; Zimmermann et al., 2011). Simulations showed that both age-related factors affected the crack growth in the tissue, which resulted in straighter cracks propagating through osteons instead of deflecting along the cement lines (Figure 5.9). The simulated fracture patterns corresponded well to crack paths in old bone reported from experiments (Chan et al., 2009). However, alterations in porosity and fracture toughness had different effects on the mechanical behavior of the simulated bone tissue, where porous models displayed a ductile behavior before failure while models with low fracture energy resulted in brittle failure (Figure 5.9). An important step was taken in study IV by demonstrating that the interface damage model was applicable also

to more complex geometries with multiple osteons and crack propagation was simulated in models with up to 15 osteons. Furthermore, by restricting the description of the bone tissue to the radial direction (instead of longitudinal or transversal osteons as in study II), the effect of the Haversian canals could also be analyzed, which was only done briefly in study II.

Realistic microstructures are necessary for patient-specific bone models. However, the computational cost of simulating crack propagation in microstructural models, even in 2D, is very high and a refined mesh is needed to discretize the thin (<5μm) cement line structures. A new strategy for representing cortical bone at the mesoscale was therefore presented in study V, where the distribution of weak interfaces was mapped from micro-CT images. Using this approach, the number of elements was reduced from approximately 330 000 in a microstructural model to roughly 20 000 in the image-based mesoscale model. The mesoscale models predicted similar crack paths and mechanical behavior as the microstructural models (Figure 5.10). The computing time for mesoscale models was also reduced to less than an hour compared to several days of wall-time used for the microstructural model. The assumption that cortical bone can be modelled as a solid with weak interfaces is supported by the analysis in study III, which showed that the cement line damage properties in combination with the strain energy release rate in the matrix were most important for the resulting crack pattern while osteon properties had a negligible effect. The crack paths simulated in mesoscale models based on micro-CT images from study I (Figure 5.11) showed good agreement with the experimental results (Figure 5.1) and highlighted the importance of the microstructure for the irregularity of the crack surface. As a consequence, a higher peak force was predicted in the longitudinal compared to the transversal model. This agreed with the experimental results (Table 5.2). The value of the simulated peak force increased further with weaker interfaces. Using baseline parameters, the normalized crack paths of both transversal and longitudinal models were underestimated compared to the experimental results (Table 5.2). However, the difference in crack length between longitudinal and transversal samples was comparable (~8% in the experiments and ~6% in the mesoscale models, based on the values “Crack length normalized with shortest crack distance” in Table 5.2)

6.2.1 Model limitations

To model crack propagation in cortical bone, the key features at the hierarchical level of interest need to be identified, as the real structure is far too complex to model. In the microstructural models in studies II-IV, the cement line was the only structure described with interface properties, as this has been shown in experiments to be crucial for deflecting cracks (Chan et al., 2009; Koester et al., 2011; O'Brien

et al., 2007), whereas both osteons and the interstitial bone matrix were assumed to be homogeneous. Resolving the lamellar structure of the osteonal and matrix tissues, including the interfaces separating them, could give a more nuanced picture of crack propagation in and around osteons by providing more weak crack paths as seen experimentally (Katsamenis et al., 2015; Peterlik et al., 2006). However, this comes at a high computational cost and would only be feasible for small model domains. Instead, the level of detail was further reduced in the image-based mesoscale models in study V, where the vascular network was used to define the distribution of weak interfaces in a homogeneous matrix. For a more detailed description of the tissue in the mesoscale models, the heterogeneity could be added by calculating the local stiffness based on the grayscale values in micro-CT images as commonly used for organ scale models (Helgason et al., 2016; Taddei et al., 2007). This approach has yet to be tested.

Simplified material descriptions were used, assuming isotropic linear elastic behavior for each component. Intrinsic mechanisms occurring in front of the crack tip, e.g. micro-cracking or diffuse damage, were captured implicitly by the cohesive damage law. A plastic material model could be used to better describe inelastic deformations occurring at smaller length scales away from the crack tip. With the current approach, the XFEM model mainly captured extrinsic toughening mechanisms taking place at the microscale, such as crack deflections. Furthermore, cortical bone is anisotropic due to the parallel arrangement of mineralized fibers at the sub-microscale, and an orthotropic material stiffness could introduce the underlying fiber orientations in longitudinal and transversal models.

Damage initiation was assumed to be strain-driven in cortical bone. This is supported by e.g. the experimental work by Nalla et al. (2003). One advantage with using a strain-based damage model is that it can be directly correlated to many experimental techniques that measure deformation (strain) locally at different length scales, e.g. digital image correlation at the tissue scale and small/wide-angle x-ray scattering at the nanoscale as used in study I. A linear softening behavior was assumed for the traction-separation law used to describe the damage evolution inside the crack. Equal strain energy release rates were assumed for all constituents as separate values are missing in experimental literature. The results from study III and study IV, show that the magnitude of the strain energy release rate had large impact on the fracture pattern, while variations in the individual parameters (i.e. $G_{cl} \neq G_{ost} \neq G_{mat}$) had negligible effects. Furthermore, cohesive laws including mixed-mode loading might be more appropriate to describe the complex crack opening in cortical bone, especially for the loading conditions occurring in vivo. So far, experimental characterization of mixed-mode damage has only been assessed as average values at the tissue scale (Zimmermann et al., 2009; Zimmermann et al., 2010). Furthermore, idealized boundary conditions were used

for all simulations presented in this thesis, restricting the analysis to uniaxial tension inspired by the experimental setup in study I.

6.2.2 The use of XFEM

The XFEM framework provides a powerful tool for simulating complex crack paths and was a key ingredient for analyzing the influence of structural and material parameters on crack propagation in cortical bone in this thesis. The possibility to simulate crack paths not known a priori is very beneficial compared to using cohesive elements that are restricted to a predefined crack path, as in (Mischinski and Ural, 2011). In comparison, the XFEM models provide a more nuanced picture with complex crack paths (see e.g. Figure 5.9 and Figure 5.11).

The XFEM formulation used in this thesis was limited to one crack, and hence new cracks were not allowed to nucleate even though a damage initiation criterion was fulfilled in an element away from the crack tip. The impact of this model assumption is difficult to evaluate, especially in models including Haversian canals. On the one hand, the limitation to one crack probably results in an over-estimation of the structural stiffness of the model, but on the other hand the unrealistic scenario with cracks nucleating inside all Haversian canals, as seen e.g. in the models by (Budyn and Hoc, 2012), is avoided. The mechanisms by which the Haversian canal is protected from crack nucleation in cortical bone tissue are not well understood, but the lamellar structure inside the osteons is believed to be crucial (Wagermaier et al., 2006; Wagermaier et al., 2015). As seen in study IV, increased porosity resulted in a ductile response before fracture and not brittle failure as reported for old porous bone (Chan et al., 2009). This model response could be due to the limitation of one crack and imaging techniques with higher temporal and spatial resolution (as used in e.g. (Zhai et al., 2019)) could possibly clarify the link between porosity and crack nucleation and growth at the microscale in young and old bone. The description of the canals as very soft solids instead of empty pores was also due to the limitation of one crack, as crack nucleation across the Haversian canal could not be initialized until the crack segment leading up to the canal was completely open. The effect of the canal stiffness was however assumed to be negligible for the mechanical performance of the models.

The mesh sensitivity analysis performed in study II showed that crack paths simulated with microstructural osteon models were surprisingly insensitive to the mesh density in the interface (Figure 5.5). Still, at least two elements were used to discretize the cement lines in all models. Numerical problems caused by mesh distortions were found to be most severe in early Abaqus versions (Figure 5.4), and Abaqus v2017 was therefore used for all simulations. Still, numerical problems occurred sporadically if the crack split the element in too close proximity to one

of the nodes. This problem was addressed by introducing the average normal in increments when the damage criteria changed from MAXPE to QUADE (Figure 5.5D), as the crack was then slightly redirected and pushed away from the element edges. This feature also improved the stability of the models by smoothing the crack path.

An initial crack was predefined in all XFEM models, as cracks would otherwise have nucleated at the edges where the boundary conditions were assigned. The use of an initial crack in an XFEM model is hence an easy way to control the location for crack growth, and the same effect is achieved when introducing a sharp notch in a specimen used in experiments. For model geometries with different shapes (i.e. not a square), crack initiation could be captured without predefined initial cracks, e.g. by using the same sample geometry as the experimental specimens in study I. This approach requires very small time-steps to avoid cracks nucleating in multiple neighboring elements, as this would cause numerical difficulties if those cracks start to intersect.

6.2.3 2D vs 3D analysis

Cortical bone has an intricate structure and the availability of high-resolution tomographic imaging techniques has shifted the gold standard for structural characterization from 2D to 3D (Muller, 2009). Three-dimensional FE-models are well-established tools for evaluating the mechanical performance of bone and with the development of image analysis schemes in 3D, e.g. digital volume correlation, the prediction of local deformation in such models can be validated to experimental data (Roberts et al., 2014). For the analysis of crack nucleation and growth in bone, a combination of 2D and 3D techniques is typically used. The standard protocols for measuring the fracture toughness (e.g. ASTM E399 and E1820) are based on analyses assuming plane strain conditions. This type of experiment is often combined with high-resolution imaging in 2D (Chan et al., 2009) or 3D (Koester et al., 2008; Koester et al., 2011; Nalla et al., 2006) to supplement the fracture toughness measurements with observations of active toughening mechanisms along the crack surface.

Simulating complex crack paths in 3D is highly challenging, as described in section 3.3, and microscale XFEM models used to model crack growth in cortical bone are in practice restricted to 2D. The interface damage model presented in this thesis can be generalized to 3D by adding the contribution from the second shear ε_t direction to the QUADE criterion as

$$f_{QUADE} = \left\{\frac{\langle \varepsilon_n \rangle}{\varepsilon_n^0}\right\}^2 + \left\{\frac{\varepsilon_s}{\varepsilon_s^0}\right\}^2 + \left\{\frac{\varepsilon_t}{\varepsilon_t^0}\right\}^2 \quad (13)$$

and by calculating the maximum principal strain based on the 3D strain tensor. For test purposes, the 3D-version of the model has been applied to a simple geometry comprising one osteon. Crack deflection was predicted in the cement line interface (Figure 6.1), and the 3D model was consistent with the models in 2D. This example illustrates that it is possible to simulate crack propagation in this type of highly simplified models, but the computational cost is high, partly due to the large number of elements needed to discretize the microstructure, and the convergence is challenging. Hence, it is currently not feasible to use this approach to simulate crack propagation in 3D models with realistic microstructures. Instead, an approach similar to the image-based mesoscale model introduced in study V could be an option to simplify the representation of the tissue structure, but the feasibility of that strategy remains to be tested.

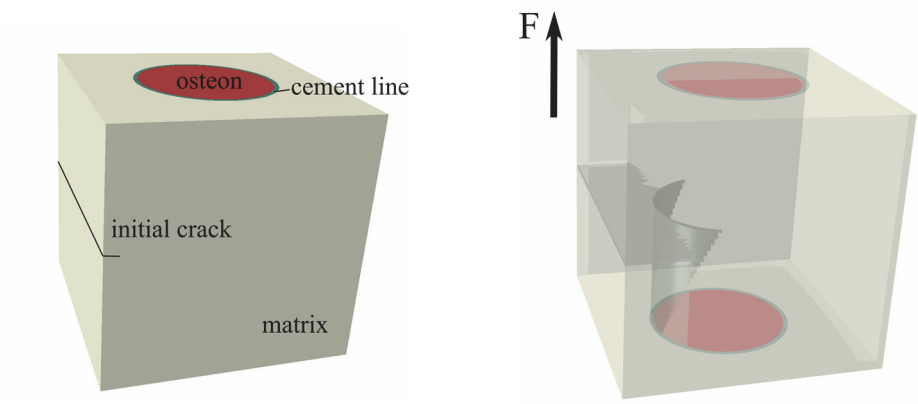

Figure 6.1. Demonstration of the interface damage model in 3D, where the crack was predicted to deflect along the cement line interface.

In the meantime, 2D models can provide useful information about crack propagation in cortical bone and the work presented in this thesis showed that different modelling strategies can be used for different applications. For instance, osteons including Haversian canals can be represented in 2D at the microscale using radial models (study II and IV). However, in longitudinal and transversal microstructural models the Haversian canals introduce exaggerated weakness and these structures are therefore better represented by solid osteons in 2D (study II and III). At the mesoscale, transversal and longitudinal microstructures are well captured using image-based models (study V). However, this approach is not suitable for modelling of radial samples, as no information about the fiber orientation is available when the fibers run in the out of plane direction (see e.g. Figure 4C in paper I).

7 Outlook

7.1 The near future

The natural continuation of this thesis work is to follow the direction taken in the last study and further validate the interface damage model against experimental data. Up to this point, the model validation has been limited to qualitative comparisons against experimental observations. This is primarily because geometries simple enough to model are difficult to machine and test experimentally, and the full complexity of biological bone samples is too complicated to model. Using the image-based modelling approach presented in study V could enable a closer comparison between models and experiments and inverse methods have potential in extracting useful information about local material parameters. Furthermore, setting up an experiment with young and old bone tissue for in situ testing at a synchrotron facility would provide a data set for model validation to better understand the capabilities and limitations of the modelling approach used in study IV.

An important step taken in study V was the image-based description of the microstructure which enabled an automatic generation of realistic mesoscale models. It is essential to develop efficient computational models and a necessary step in order to simulate complex phenomena in 3D. Exploring possibilities beyond XFEM for modeling of interface damage in 3D is therefore also part of future goals. Phase-field models are interesting candidates, as they are expected to be less restricted for 3D applications compared to XFEM (Miehe et al., 2010; Raina and Miehe, 2016). The work by Hansen-Dorr et al. (2019) for interface damage would then be a natural starting point for applying phase-field models to cortical bone.

7.2 The far future

Many of the challenges for modeling crack growth in cortical bone tissue have already been discussed in the previous sections, e.g. the problems with 3D models and the need of better experimental characterization of local material parameters. As pointed out in the introduction, a comprehensive understanding of the underlying damage mechanisms in bone is key to develop reliable predictive tools for fracture risk assessment in a clinical setting. An important aspect will be to go beyond quasi-static models, to try to simulate also the distinct scenarios of fatigue induced damage or fractures from impact loading. This is necessary to capture clinically relevant fracture scenarios. Furthermore, a main challenge for future studies is the development of multiscale models to capture the hierarchical structure of bone. Full multiscale models are still out of reach, but improved understanding of e.g. load transfer between different hierarchical levels is crucial to elucidate the underlying mechanisms for both damage initiation and growth. To succeed, a stochastic description might be needed to capture the random nature of damage and the heterogeneity and local imperfections in bone. Finally, the ultimate task remains, to bridge the gap between bone mechanics and the prediction of fracture risk for individual patients in the clinic in order to identify patients at risk and, more importantly, prevent subsequent fractures. Clearly, a multidisciplinary research effort is needed to face this challenge.

8 Summary and conclusions

In this thesis, a combination of experimental and numerical techniques was used to analyze the role of microstructure for crack propagation in cortical bone. A key component was the development of an XFEM interface damage model that could capture realistic crack paths in cortical bone at micro- and mesoscales. The major scientific findings of this thesis can be summarized as:

- Strains at both tissue- and nanoscale in cortical bone depend on the microstructure.
- Fracture paths in cortical bone follow the microstructure and the irregularity of the crack surface increases when the crack propagates perpendicular instead of parallel to the material orientation.
- The interface strength and the strain energy release rate of the bone tissue both influence the capability of the cement line to deflect cracks.
- The osteonal microstructure affects propagating cracks through two distinct mechanisms: Haversian canals attract cracks and cement lines deflect cracks.
- Both increased porosity and decreased fracture toughness promote crack penetration of osteons. However, only decreased fracture toughness results in a brittle failure.
- Weaker interfaces result in increased crack irregularity and higher peak force when cracks propagate perpendicular to the microstructure.

References

ABAQUS/Standard, 2017. SIMULIA User Assistance v2017. Dassault Systemes.

Abdel-Wahab, A.A., Maligno, A.R., Silberschmidt, V.V., 2012. Micro-scale modelling of bovine cortical bone fracture: Analysis of crack propagation and microstructure using X-FEM. Computational Materials Science 52, 128-135.

Acerbo, A.S., Kwaczala, A.T., Yang, L., Judex, S., Miller, L.M., 2014. Alterations in collagen and mineral nanostructure observed in osteoporosis and pharmaceutical treatments using simultaneous small- and wide-angle X-ray scattering. Calcif Tissue Int 95, 446-456.

Acevedo, C., Stadelmann, V.A., Pioletti, D.P., Alliston, T., Ritchie, R.O., 2018. Fatigue as the missing link between bone fragility and fracture. Nat Biomed Eng 2, 62-71.

Agnew, A.M., Dominguez, V.M., Sciulli, P.W., Stout, S.D., 2017. Variability of in vivo linear microcrack accumulation in the cortex of elderly human ribs. Bone Rep 6, 60-63.

Ali, A.A., Cristofolini, L., Schileo, E., Hu, H., Taddei, F., Kim, R.H., Rullkoetter, P.J., Laz, P.J., 2014. Specimen-specific modeling of hip fracture pattern and repair. J Biomech 47, 536-543.

An, B., Zhang, D., 2018. An analysis of crack growth in dentin at the microstructural scale. J Mech Behav Biomed Mater 81, 149-160.

Aspenberg, P., Schilcher, J., 2014. Atypical femoral fractures, bisphosphonates, and mechanical stress. Curr Osteoporos Rep 12, 189-193.

Baptista, R., Almeida, A., Infante, V., 2016. Micro-crack propagation on a biomimetic bone like composite material studied with the extended finite element method. Xv Portuguese Conference on Fracture, Pcf 2016 1, 18-25.

Barenblatt, G.I., 1959. The formation of equilibrium cracks during brittle fracture. General ideas and hypotheses. Axially-symmetric cracks. Journal of Applied Mathematics and Mechanics 23, 622-636.

Belytschko, T., Black, T., 1999. Elastic crack growth in finite elements with minimal remeshing. Int J Numer Meth Eng 45, 601-620.

Bettamer, A., Hambli, R., Allaoui, S., Almhdie-Imjabber, A., 2017. Using visual image measurements to validate a novel finite element model of crack propagation and fracture patterns of proximal femur. Comp M Bio Bio E-Iv 5, 251-262.

Bigley, R.F., Griffin, L.V., Christensen, L., Vandenbosch, R., 2006. Osteon interfacial strength and histomorphometry of equine cortical bone. J Biomech 39, 1629-1640.

Boskey, A.L., Imbert, L., 2017. Bone quality changes associated with aging and disease: a review. Ann N Y Acad Sci 1410, 93-106.

Bourdin, B., Francfort, G.A., Marigo, J.J., 2000. Numerical experiments in revisited brittle fracture. J Mech Phys Solids 48, 797-826.

Bourdin, B., Francfort, G.A., Marigo, J.J., 2008. The variational approach to fracture. J Elasticity 91, 5-148.

Bouxsein, M.L., Boyd, S.K., Christiansen, B.A., Guldberg, R.E., Jepsen, K.J., Muller, R., 2010. Guidelines for assessment of bone microstructure in rodents using micro-computed tomography. J Bone Miner Res 25, 1468-1486.

Brekelmans, W.A.M., Devree, J.H.P., 1995. Reduction of Mesh Sensitivity in Continuum Damage Mechanics. Acta Mechanica 110, 49-56.

Budhe, S., Banea, M.D., de Barros, S., da Silva, L.F.M., 2017. An updated review of adhesively bonded joints in composite materials. International Journal of Adhesion and Adhesives 72, 30-42.

Budyn, E., Hoc, T., 2010. Analysis of micro fracture in human Haversian cortical bone under transverse tension using extended physical imaging. Int J Numer Meth Eng 82, 940-965.

Budyn, É., Hoc, T., 2012. Multiple scale modeling for cortical bone fracture in tension using X-FEM. European Journal of Computational Mechanics 16, 213-236.

Budyn, E., Hoc, T., Jonvaux, J., 2008. Fracture strength assessment and aging signs detection in human cortical bone using an X-FEM multiple scale approach. Computational Mechanics 42, 579-591.

Budyn, E., Jonvaux, J., Hoc, T., 2012. Digital image correlation of bone sequential microscopic observations. Int J Numer Meth Bio 28, 815-837.

Burr, D.B., 2004. Bone quality: understanding what matters. J Musculoskelet Neuronal Interact 4, 184-186.

Burr, D.B., 2019. Changes in bone matrix properties with aging. Bone 120, 85-93.

Burr, D.B., Schaffler, M.B., Frederickson, R.G., 1988. Composition of the cement line and its possible mechanical role as a local interface in human compact bone. Journal of Biomechanics 21, 939-945.

Chan, K.S., Chan, C.K., Nicolella, D.P., 2009. Relating crack-tip deformation to mineralization and fracture resistance in human femur cortical bone. Bone 45, 427-434.

Cook, J., Gordon, J., Year A mechanism for the control of crack propagation in all-brittle systems. In Proc. R. Soc. Lond. A.

Cooper, D.M., Thomas, C.D., Clement, J.G., Turinsky, A.L., Sensen, C.W., Hallgrimsson, B., 2007. Age-dependent change in the 3D structure of cortical porosity at the human femoral midshaft. Bone 40, 957-965.

De Borst, R., 2003. Numerical aspects of cohesive-zone models. Engineering fracture mechanics 70, 1743-1757.

Demirtas, A., Curran, E., Ural, A., 2016. Assessment of the effect of reduced compositional heterogeneity on fracture resistance of human cortical bone using finite element modeling. Bone 91, 92-101.

Demirtas, A., Ural, A., 2018a. Interaction of Microcracks and Tissue Compositional Heterogeneity in Determining Fracture Resistance of Human Cortical Bone. J Biomech Eng 140.

Demirtas, A., Ural, A., 2018b. Material heterogeneity, microstructure, and microcracks demonstrate differential influence on crack initiation and propagation in cortical bone. Biomech Model Mechanobiol 17, 1415-1428.

Diab, T., Vashishth, D., 2007. Morphology, localization and accumulation of in vivo microdamage in human cortical bone. Bone 40, 612-618.

Donaldson, F., Ruffoni, D., Schneider, P., Levchuk, A., Zwahlen, A., Pankaj, P., Muller, R., 2014. Modeling microdamage behavior of cortical bone. Biomech Model Mechanobiol 13, 1227-1242.

Dong, X.N., Zhang, X., Guo, X.E., 2005. Interfacial strength of cement lines in human cortical bone. Mech Chem Biosyst 2, 63-68.

Dourado, N., Pereira, F.A., de Moura, M.F., Morais, J.J., Dias, M.I., 2013. Bone fracture characterization using the end notched flexure test. Mater Sci Eng C Mater Biol Appl 33, 405-410.

Engqvist, J., Hall, S.A., Wallin, M., Ristinmaa, M., Plivelic, T.S., 2014. Multi-scale Measurement of (Amorphous) Polymer Deformation: Simultaneous X-ray Scattering, Digital Image Correlation and In-situ Loading. Experimental Mechanics 54, 1373-1383.

Faingold, A., Cohen, S.R., Shahar, R., Weiner, S., Rapoport, L., Wagner, H.D., 2014. The effect of hydration on mechanical anisotropy, topography and fibril organization of the osteonal lamellae. J Biomech 47, 367-372.

Fantner, G.E., Hassenkam, T., Kindt, J.H., Weaver, J.C., Birkedal, H., Pechenik, L., Cutroni, J.A., Cidade, G.A., Stucky, G.D., Morse, D.E., Hansma, P.K., 2005.

Sacrificial bonds and hidden length dissipate energy as mineralized fibrils separate during bone fracture. Nat Mater 4, 612-616.

Feerick, E.M., Liu, X.C., McGarry, P., 2013. Anisotropic mode-dependent damage of cortical bone using the extended finite element method (XFEM). J Mech Behav Biomed Mater 20, 77-89.

Feik, S.A., Thomas, C.D., Clement, J.G., 1997. Age-related changes in cortical porosity of the midshaft of the human femur. J Anat 191 (Pt 3), 407-416.

Frasca, P., 1981. Scanning-electron microscopy studies of 'ground substance' in the cement lines, resting lines, hypercalcified rings and reversal lines of human cortical bone. Acta Anat (Basel) 109, 115-121.

Gargac, J.A., Turnbull, T.L., Roeder, R.K., Niebur, G.L., 2014. A probabilistic damage model based on direct 3-D correlation of strain to damage formation following fatigue loading of rat femora. J Mech Behav Biomed Mater 30, 234-243.

Gasser, T.C., Holzapfel, G.A., 2006. 3D Crack propagation in unreinforced concrete. A two-step algorithm for tracking 3D crack paths. Comput Method Appl M 195, 5198-5219.

Gasser, T.C., Holzapfel, G.A., 2007. A numerical framework to model 3-D fracture in bone tissue with application to failure of the proximal femur. Iutam Bookser 5, 199.

Giner, E., Belda, R., Arango, C., Vercher-Martínez, A., Tarancón, J.E., Fuenmayor, F.J., 2017. Calculation of the critical energy release rate Gc of the cement line in cortical bone combining experimental tests and finite element models. Engineering Fracture Mechanics 184, 168-182.

Granke, M., Makowski, A.J., Uppuganti, S., Does, M.D., Nyman, J.S., 2015. Identifying Novel Clinical Surrogates to Assess Human Bone Fracture Toughness. J Bone Miner Res 30, 1290-1300.

Granke, M., Makowski, A.J., Uppuganti, S., Nyman, J.S., 2016. Prevalent role of porosity and osteonal area over mineralization heterogeneity in the fracture toughness of human cortical bone. J Biomech 49, 2748-2755.

Grassi, L., Isaksson, H., 2015. Extracting accurate strain measurements in bone mechanics: A critical review of current methods. Journal of the Mechanical Behavior of Biomedical Materials 50, 43-54.

Griffith, A.A., 1968. Phenomena of Rupture and Flow in Solids. Asm Trans Q 61, 871.

Gross, D., Seelig, T., 2017. Fracture mechanics: with an introduction to micromechanics. Springer.

Gultekin, O., Dal, H., Holzapfel, G.A., 2016. A phase-field approach to model fracture of arterial walls: Theory and finite element analysis. Comput Methods Appl Mech Eng 312, 542-566.

Gultekin, O., Dal, H., Holzapfel, G.A., 2017. Crack Phase-Field Modeling of Anisotropic Rupture in Fibrous Soft Tissues. Computational Plasticity Xiv: Fundamentals and Applications, 139-150.

Gultekin, O., Dal, H., Holzapfel, G.A., 2018. Numerical aspects of anisotropic failure in soft biological tissues favor energy-based criteria: A rate-dependent anisotropic crack phase-field model. Comput Methods Appl Mech Eng 331, 23-52.

Gupta, H.S., Seto, J., Wagermaier, W., Zaslansky, P., Boesecke, P., Fratzl, P., 2006a. Cooperative deformation of mineral and collagen in bone at the nanoscale. P Natl Acad Sci USA 103, 17741-17746.

Gupta, H.S., Stachewicz, U., Wagermaier, W., Roschger, P., Wagner, H.D., Fratzl, P., 2006b. Mechanical modulation at the lamellar level in osteonal bone. J Mater Res 21, 1913-1921.

Gupta, H.S., Wagermaier, W., Zickler, G.A., Hartmann, J., Funari, S.S., Roschger, P., Wagner, H.D., Fratzl, P., 2006c. Fibrillar level fracture in bone beyond the yield point. International Journal of Fracture 139, 425-436.

Gustafsson, A., Mathavan, N., Turunen, M.J., Engqvist, J., Khayyeri, H., Hall, S.A., Isaksson, H., 2018. Linking multiscale deformation to microstructure in cortical bone using in situ loading, digital image correlation and synchrotron X-ray scattering. Acta Biomater 69, 323-331.

Haider, I.T., Goldak, J., Frei, H., 2018. Femoral fracture load and fracture pattern is accurately predicted using a gradient-enhanced quasi-brittle finite element model. Med Eng Phys 55, 1-8.

Hambli, R., 2013. A quasi-brittle continuum damage finite element model of the human proximal femur based on element deletion. Med Biol Eng Comput 51, 219-231.

Hambli, R., Bettamer, A., Allaoui, S., 2012. Finite element prediction of proximal femur fracture pattern based on orthotropic behaviour law coupled to quasi-brittle damage. Med Eng Phys 34, 202-210.

Hammond, M.A., Wallace, J.M., Allen, M.R., Siegmund, T., 2019. Mechanics of linear microcracking in trabecular bone. J Biomech 83, 34-42.

Hansen-Dorr, A.C., de Borst, R., Hennig, P., Kastner, M., 2019. Phase-field modelling of interface failure in brittle materials. Comput Method Appl M 346, 25-42.

Hashin, Z., 1980. Failure Criteria for Unidirectional Fiber Composites. J Appl Mech-T Asme 47, 329-334.

He, M.Y., Hutchinson, J.W., 1989. Crack Deflection at an Interface between Dissimilar Elastic-Materials. Int J Solids Struct 25, 1053-1067.

Helgason, B., Gilchrist, S., Ariza, O., Vogt, P., Enns-Bray, W., Widmer, R.P., Fitze, T., Palsson, H., Pauchard, Y., Guy, P., Ferguson, S.J., Cripton, P.A., 2016. The influence of the modulus-density relationship and the material mapping method on

the simulated mechanical response of the proximal femur in side-ways fall loading configuration. Med Eng Phys 38, 679-689.

Hengsberger, S., Kulik, A., Zysset, P., 2002. Nanoindentation discriminates the elastic properties of individual human bone lamellae under dry and physiological conditions. Bone 30, 178-184.

Hernandez, C.J., Keaveny, T.M., 2006. A biomechanical perspective on bone quality. Bone 39, 1173-1181.

Hernandez, C.J., van der Meulen, M.C., 2017. Understanding Bone Strength Is Not Enough. J Bone Miner Res 32, 1157-1162.

Hernlund, E., Svedbom, A., Ivergard, M., Compston, J., Cooper, C., Stenmark, J., McCloskey, E.V., Jonsson, B., Kanis, J.A., 2013. Osteoporosis in the European Union: medical management, epidemiology and economic burden. A report prepared in collaboration with the International Osteoporosis Foundation (IOF) and the European Federation of Pharmaceutical Industry Associations (EFPIA). Arch Osteoporos 8, 136.

Hui, S.L., Slemenda, C.W., Johnston, C.C., Jr., 1988. Age and bone mass as predictors of fracture in a prospective study. J Clin Invest 81, 1804-1809.

Idkaidek, A., Jasiuk, I., 2017. Cortical bone fracture analysis using XFEM - case study. Int J Numer Method Biomed Eng 33.

Idkaidek, A., Koric, S., Jasiuk, I., 2017. Fracture analysis of multi-osteon cortical bone using XFEM. Computational Mechanics 62, 171-184.

Isaksson, H., van Donkelaar, C.C., Huiskes, R., Yao, J., Ito, K., 2008. Determining the most important cellular characteristics for fracture healing using design of experiments methods. J Theor Biol 255, 26-39.

Iwamoto, J., Takeda, T., 2003. Stress fractures in athletes: review of 196 cases. J Orthop Sci 8, 273-278.

Johannesdottir, F., Allaire, B., Bouxsein, M.L., 2018. Fracture Prediction by Computed Tomography and Finite Element Analysis: Current and Future Perspectives. Curr Osteoporos Rep 16, 411-422.

Jones, B.H., Thacker, S.B., Gilchrist, J., Kimsey, C.D., Jr., Sosin, D.M., 2002. Prevention of lower extremity stress fractures in athletes and soldiers: a systematic review. Epidemiol Rev 24, 228-247.

Kanis, J.A., Cooper, C., Rizzoli, R., Reginster, J.Y., Scientific Advisory Board of the European Society for, C., Economic Aspects of, O., the Committees of Scientific, A., National Societies of the International Osteoporosis, F., 2019. European guidance for the diagnosis and management of osteoporosis in postmenopausal women. Osteoporos Int 30, 3-44.

Kanis, J.A., Johnell, O., Oden, A., Johansson, H., McCloskey, E., 2008. FRAX and the assessment of fracture probability in men and women from the UK. Osteoporos Int 19, 385-397.

Karunaratne, A., Terrill, N.J., Gupta, H.S., 2013. Synchrotron X-ray nanomechanical imaging of mineralized fiber composites. Methods Enzymol 532, 415-473.

Kataruka, A., Mendu, K., Okeoghene, O., Puthuvelil, J., Akono, A.-T., 2017. Microscopic assessment of bone toughness using scratch tests. Bone reports 6, 17-25.

Katsamenis, O.L., Jenkins, T., Quinci, F., Michopoulou, S., Sinclair, I., Thurner, P.J., 2013. A novel videography method for generating crack-extension resistance curves in small bone samples. Plos One 8, e55641.

Katsamenis, O.L., Jenkins, T., Thurner, P.J., 2015. Toughness and damage susceptibility in human cortical bone is proportional to mechanical inhomogeneity at the osteonal-level. Bone 76, 158-168.

Kennedy, O.D., Brennan, O., Mauer, P., Rackard, S.M., O'Brien, F.J., Taylor, D., Lee, T.C., 2008. The effects of increased intracortical remodeling on microcrack behaviour in compact bone. Bone 43, 889-893.

Kerschnitzki, M., Wagermaier, W., Roschger, P., Seto, J., Shahar, R., Duda, G.N., Mundlos, S., Fratzl, P., 2011. The organization of the osteocyte network mirrors the extracellular matrix orientation in bone. J Struct Biol 173, 303-311.

Khoei, A.R., 2014. Extended finite element method: theory and applications. John Wiley & Sons.

Koester, K.J., Ager, J.W., 3rd, Ritchie, R.O., 2008. The true toughness of human cortical bone measured with realistically short cracks. Nat Mater 7, 672-677.

Koester, K.J., Barth, H.D., Ritchie, R.O., 2011. Effect of aging on the transverse toughness of human cortical bone: evaluation by R-curves. J Mech Behav Biomed Mater 4, 1504-1513.

Kruzic, J.J., Kim, D.K., Koester, K.J., Ritchie, R.O., 2009. Indentation techniques for evaluating the fracture toughness of biomaterials and hard tissues. J Mech Behav Biomed Mater 2, 384-395.

Labrador, A., Cerenius, Y., Svensson, C., Theodor, K., Plivelic, T., Year The yellow mini-hutch for SAXS experiments at MAX IV Laboratory. In Journal of Physics: Conference Series.

Langer, M., Pacureanu, A., Suhonen, H., Grimal, Q., Cloetens, P., Peyrin, F., 2012. X-ray phase nanotomography resolves the 3D human bone ultrastructure. Plos One 7, e35691.

Launey, M.E., Buehler, M.J., Ritchie, R.O., 2010. On the Mechanistic Origins of Toughness in Bone. Annu Rev Mater Res 40, 25-53.

Lespessailles, E., Chappard, C., Bonnet, N., Benhamou, C.L., 2006. Imaging techniques for evaluating bone microarchitecture. Joint Bone Spine 73, 254-261.

Li, S.M., Abdel-Wahab, A., Demirci, E., Silberschmidt, V.V., 2013. Fracture process in cortical bone: X-FEM analysis of microstructured models. International Journal of Fracture 184, 43-55.

Lin, Z.X., Xu, Z.H., An, Y.H., Li, X., 2016. In situ observation of fracture behavior of canine cortical bone under bending. Mater Sci Eng C Mater Biol Appl 62, 361-367.

Lipson, S.F., Katz, J.L., 1984. The Relationship between Elastic Properties and Microstructure of Bovine Cortical Bone. Journal of Biomechanics 17, 231.

Liu, X.C., Qin, X., Du, Z.-z., Year Bone fracture analysis using the extended finite element method (XFEM) with abaqus. In The 34th annual meeting of the American society of biomechanics.

Luo, Q., Nakade, R., Dong, X., Rong, Q., Wang, X., 2011. Effect of mineral-collagen interfacial behavior on the microdamage progression in bone using a probabilistic cohesive finite element model. J Mech Behav Biomed Mater 4, 943-952.

Maghsoudi-Ganjeh, M., Lin, L., Wang, X., Zeng, X., 2019. Computational investigation of ultrastructural behavior of bone using a cohesive finite element approach. Biomech Model Mechanobiol 18, 463-478.

Malo, M.K., Rohrbach, D., Isaksson, H., Toyras, J., Jurvelin, J.S., Tamminen, I.S., Kroger, H., Raum, K., 2013. Longitudinal elastic properties and porosity of cortical bone tissue vary with age in human proximal femur. Bone 53, 451-458.

Marco, M., Belda, R., Miguelez, M.H., Giner, E., 2018a. A heterogeneous orientation criterion for crack modelling in cortical bone using a phantom-node approach. Finite Elem Anal Des 146, 107-117.

Marco, M., Giner, E., Caeiro-Rey, J.R., Miguelez, M.H., Larrainzar-Garijo, R., 2019. Numerical modelling of hip fracture patterns in human femur. Comput Methods Programs Biomed 173, 67-75.

Marco, M., Giner, E., Larrainzar-Garijo, R., Caeiro, J.R., Miguelez, M.H., 2018b. Modelling of femur fracture using finite element procedures. Engineering Fracture Mechanics 196, 157-167.

Martin, R.B., Gibson, V.A., Stover, S.M., Gibeling, J.C., Griffin, L.V., 1996. Osteonal structure in the equine third metacarpus. Bone 19, 165-171.

Mayya, A., Banerjee, A., Rajesh, R., 2016. Haversian microstructure in bovine femoral cortices: An adaptation for improved compressive strength. Mater Sci Eng C Mater Biol Appl 59, 454-463.

McNally, E.A., Schwarcz, H.P., Botton, G.A., Arsenault, A.L., 2012. A model for the ultrastructure of bone based on electron microscopy of ion-milled sections. Plos One 7, e29258.

Melenk, J.M., Babuska, I., 1996. The partition of unity finite element method: Basic theory and applications. Comput Method Appl M 139, 289-314.

Melton, L.J., 3rd, 1990. A "Gompertzian" view of osteoporosis. Calcif Tissue Int 46, 285-286.

Miehe, C., Welschinger, F., Hofacker, M., 2010. Thermodynamically consistent phase-field models of fracture: Variational principles and multi-field FE implementations. Int J Numer Meth Eng 83, 1273-1311.

Milovanovic, P., Vom Scheidt, A., Mletzko, K., Sarau, G., Puschel, K., Djuric, M., Amling, M., Christiansen, S., Busse, B., 2018. Bone tissue aging affects mineralization of cement lines. Bone 110, 187-193.

Mirzaali, M.J., Schwiedrzik, J.J., Thaiwichai, S., Best, J.P., Michler, J., Zysset, P.K., Wolfram, U., 2016. Mechanical properties of cortical bone and their relationships with age, gender, composition and microindentation properties in the elderly. Bone 93, 196-211.

Mirzaei, M., Alavi, F., Allaveisi, F., Naeini, V., Amiri, P., 2018. Linear and nonlinear analyses of femoral fractures: Computational/experimental study. J Biomech 79, 155-163.

Mischinski, S., Ural, A., 2011. Finite Element Modeling of Microcrack Growth in Cortical Bone. J Appl Mech-T Asme 78, 041016.

Mischinski, S., Ural, A., 2013. Interaction of microstructure and microcrack growth in cortical bone: a finite element study. Comput Methods Biomech Biomed Engin 16, 81-94.

Mohsin, S., O'Brien, F.J., Lee, T.C., 2006. Osteonal crack barriers in ovine compact bone. J Anat 208, 81-89.

Montalbano, T., Feng, G., 2011. Nanoindentation characterization of the cement lines in ovine and bovine femurs. J Mater Res 26, 1036-1041.

Montgomery, D.C., 2005. Design and analysis of experiments, Sixth ed. John wiley & sons.

Muller, R., 2009. Hierarchical microimaging of bone structure and function. Nat Rev Rheumatol 5, 373-381.

Mullins, L.P., Sassi, V., McHugh, P.E., Bruzzi, M.S., 2009. Differences in the crack resistance of interstitial, osteonal and trabecular bone tissue. Ann Biomed Eng 37, 2574-2582.

Najafi, A.R., Arshi, A.R., Eslami, M.R., Fariborz, S., Moeinzadeh, M.H., 2007. Micromechanics fracture in osteonal cortical bone: a study of the interactions between microcrack propagation, microstructure and the material properties. J Biomech 40, 2788-2795.

Nalla, R.K., Kinney, J.H., Ritchie, R.O., 2003. Mechanistic fracture criteria for the failure of human cortical bone. Nat Mater 2, 164-168.

Nalla, R.K., Kruzic, J.J., Kinney, J.H., Balooch, M., Ager, J.W., Ritchie, R.O., 2006. Role of microstructure in the aging-related deterioration of the toughness of human cortical bone. Materials Science & Engineering C-Biomimetic and Supramolecular Systems 26, 1251-1260.

Nalla, R.K., Kruzic, J.J., Kinney, J.H., Ritchie, R.O., 2004a. Effect of aging on the toughness of human cortical bone: evaluation by R-curves. Bone 35, 1240-1246.

Nalla, R.K., Kruzic, J.J., Kinney, J.H., Ritchie, R.O., 2005. Mechanistic aspects of fracture and R-curve behavior in human cortical bone. Biomaterials 26, 217-231.

Nalla, R.K., Kruzic, J.J., Ritchie, R.O., 2004b. On the origin of the toughness of mineralized tissue: microcracking or crack bridging? Bone 34, 790-798.

Nirody, J.A., Cheng, K.P., Parrish, R.M., Burghardt, A.J., Majumdar, S., Link, T.M., Kazakia, G.J., 2015. Spatial distribution of intracortical porosity varies across age and sex. Bone 75, 88-95.

Nobakhti, S., Limbert, G., Thurner, P.J., 2014. Cement lines and interlamellar areas in compact bone as strain amplifiers - contributors to elasticity, fracture toughness and mechanotransduction. J Mech Behav Biomed Mater 29, 235-251.

Norman, T.L., Vashishth, D., Burr, D.B., 1995. Fracture toughness of human bone under tension. J Biomech 28, 309-320.

Nyman, J.S., Makowski, A.J., 2012. The contribution of the extracellular matrix to the fracture resistance of bone. Curr Osteoporos Rep 10, 169-177.

Nyman, J.S., Roy, A., Shen, X., Acuna, R.L., Tyler, J.H., Wang, X., 2006. The influence of water removal on the strength and toughness of cortical bone. J Biomech 39, 931-938.

O'Brien, F.J., Taylor, D., Clive Lee, T., 2005. The effect of bone microstructure on the initiation and growth of microcracks. J Orthop Res 23, 475-480.

O'Brien, F.J., Taylor, D., Lee, T.C., 2007. Bone as a composite material: The role of osteons as barriers to crack growth in compact bone. International Journal of Fatigue 29, 1051-1056.

Oden, A., McCloskey, E.V., Johansson, H., Kanis, J.A., 2013. Assessing the Impact of Osteoporosis on the Burden of Hip Fractures. Calcified Tissue International 92, 42-49.

Parmigiani, J.P., Thouless, M.D., 2006. The roles of toughness and cohesive strength on crack deflection at interfaces. J Mech Phys Solids 54, 266-287.

Peterlik, H., Roschger, P., Klaushofer, K., Fratzl, P., 2006. From brittle to ductile fracture of bone. Nat Mater 5, 52-55.

Püspöki, Z., Storath, M., Sage, D., Unser, M., 2016. Transforms and operators for directional bioimage analysis: a survey, Focus on Bio-Image Informatics. Springer, pp. 69-93.

Rabczuk, T., 2013. Computational methods for fracture in brittle and quasi-brittle solids: state-of-the-art review and future perspectives. ISRN Applied Mathematics 2013.

Raeisi Najafi, A., Arshi, A.R., Saffar, K.P., Eslami, M.R., Fariborz, S., Moeinzadeh, M.H., 2009. A fiber-ceramic matrix composite material model for osteonal cortical bone fracture micromechanics: solution of arbitrary microcracks interaction. J Mech Behav Biomed Mater 2, 217-223.

Raina, A., Miehe, C., 2016. A phase-field model for fracture in biological tissues. Biomech Model Mechanobiol 15, 479-496.

Reznikov, N., Bilton, M., Lari, L., Stevens, M.M., Kroger, R., 2018. Fractal-like hierarchical organization of bone begins at the nanoscale. Science 360.

Rho, J.Y., Zioupos, P., Currey, J.D., Pharr, G.M., 1999. Variations in the individual thick lamellar properties within osteons by nanoindentation. Bone 25, 295-300.

Rho, J.Y., Zioupos, P., Currey, J.D., Pharr, G.M., 2002. Microstructural elasticity and regional heterogeneity in human femoral bone of various ages examined by nano-indentation. Journal of Biomechanics 35, 189-198.

Rinnerthaler, S., Roschger, P., Jakob, H.F., Nader, A., Klaushofer, K., Fratzl, P., 1999. Scanning small angle X-ray scattering analysis of human bone sections. Calcif Tissue Int 64, 422-429.

Ritchie, R.O., 1999. Mechanisms of fatigue-crack propagation in ductile and brittle solids. International Journal of Fracture 100, 55-83.

Roberts, B.C., Perilli, E., Reynolds, K.J., 2014. Application of the digital volume correlation technique for the measurement of displacement and strain fields in bone: a literature review. J Biomech 47, 923-934.

Rodriguez-Florez, N., Carriero, A., Shefelbine, S.J., 2017. The use of XFEM to assess the influence of intra-cortical porosity on crack propagation. Comput Methods Biomech Biomed Engin 20, 385-392.

Sabet, F.A., Najafi, A.R., Hamed, E., Jasiuk, I., 2016. Modelling of bone fracture and strength at different length scales: a review. Interface Focus 6, 20150055.

Schaffler, M.B., Burr, D.B., Frederickson, R.G., 1987. Morphology of the osteonal cement line in human bone. Anat Rec 217, 223-228.

Schaffler, M.B., Choi, K., Milgrom, C., 1995. Aging and matrix microdamage accumulation in human compact bone. Bone 17, 521-525.

Schneider, C.A., Rasband, W.S., Eliceiri, K.W., 2012. NIH Image to ImageJ: 25 years of image analysis. Nat Methods 9, 671-675.

Schreier, H., Orteu, J.-J., Sutton, M.A., 2009. Image correlation for shape, motion and deformation measurements. Springer US.

Seref-Ferlengez, Z., Kennedy, O.D., Schaffler, M.B., 2015. Bone microdamage, remodeling and bone fragility: how much damage is too much damage [quest]. BoneKEy reports 4.

Sharir, A., Barak, M.M., Shahar, R., 2008. Whole bone mechanics and mechanical testing. Vet J 177, 8-17.

Skedros, J.G., Holmes, J.L., Vajda, E.G., Bloebaum, R.D., 2005. Cement lines of secondary osteons in human bone are not mineral-deficient: new data in a historical perspective. Anat Rec A Discov Mol Cell Evol Biol 286, 781-803.

Song, J.H., Areias, P.M.A., Belytschko, T., 2006. A method for dynamic crack and shear band propagation with phantom nodes. Int J Numer Meth Eng 67, 868-893.

Stein, M.S., Feik, S.A., Thomas, C.D., Clement, J.G., Wark, J.D., 1999. An automated analysis of intracortical porosity in human femoral bone across age. J Bone Miner Res 14, 624-632.

Sun, X., Hoon Jeon, J., Blendell, J., Akkus, O., 2010. Visualization of a phantom post-yield deformation process in cortical bone. J Biomech 43, 1989-1996.

Taddei, F., Schileo, E., Helgason, B., Cristofolini, L., Viceconti, M., 2007. The material mapping strategy influences the accuracy of CT-based finite element models of bones: an evaluation against experimental measurements. Med Eng Phys 29, 973-979.

Tang, T., Ebacher, V., Cripton, P., Guy, P., McKay, H., Wang, R., 2015. Shear deformation and fracture of human cortical bone. Bone 71, 25-35.

Taylor, D., 2018. Measuring fracture toughness in biological materials. J Mech Behav Biomed Mater 77, 776-782.

Taylor, D., Hazenberg, J.G., Lee, T.C., 2007. Living with cracks: damage and repair in human bone. Nat Mater 6, 263-268.

Tong, X., Burton, I.S., Isaksson, H., Jurvelin, J.S., Kroger, H., 2015. Cortical bone histomorphometry in male femoral neck: the investigation of age-association and regional differences. Calcif Tissue Int 96, 295-306.

Turner, C.H., Burr, D.B., 1993. Basic biomechanical measurements of bone: a tutorial. Bone 14, 595-608.

Turunen, M.J., Kaspersen, J.D., Olsson, U., Guizar-Sicairos, M., Bech, M., Schaff, F., Tagil, M., Jurvelin, J.S., Isaksson, H., 2016. Bone mineral crystal size and organization vary across mature rat bone cortex. J Struct Biol 195, 337-344.

Turunen, M.J., Khayyeri, H., Guizar-Sicairos, M., Isaksson, H., 2017. Effects of tissue fixation and dehydration on tendon collagen nanostructure. J Struct Biol 199, 209-215.

Turunen, M.J., Lages, S., Labrador, A., Olsson, U., Tagil, M., Jurvelin, J.S., Isaksson, H., 2014. Evaluation of composition and mineral structure of callus tissue in rat femoral fracture. J Biomed Opt 19, 025003.

Unal, M., Creecy, A., Nyman, J.S., 2018. The Role of Matrix Composition in the Mechanical Behavior of Bone. Curr Osteoporos Rep 16, 205-215.

Ural, A., Mischinski, S., 2013. Multiscale modeling of bone fracture using cohesive finite elements. Engineering Fracture Mechanics 103, 141-152.

Ural, A., Vashishth, D., 2006. Cohesive finite element modeling of age-related toughness loss in human cortical bone. J Biomech 39, 2974-2982.

Vergani, L., Colombo, C., Libonati, F., 2014. Crack propagation in cortical bone: a numerical study. 20th European Conference on Fracture 3, 1524-1529.

Viceconti, M., Qasim, M., Bhattacharya, P., Li, X., 2018. Are CT-Based Finite Element Model Predictions of Femoral Bone Strengthening Clinically Useful? Curr Osteoporos Rep 16, 216-223.

Wagermaier, W., Gupta, H.S., Gourrier, A., Burghammer, M., Roschger, P., Fratzl, P., 2006. Spiral twisting of fiber orientation inside bone lamellae. Biointerphases 1, 1.

Wagermaier, W., Klaushofer, K., Fratzl, P., 2015. Fragility of Bone Material Controlled by Internal Interfaces. Calcif Tissue Int 97, 201-212.

Wainwright, S.A., Marshall, L.M., Ensrud, K.E., Cauley, J.A., Black, D.M., Hillier, T.A., Hochberg, M.C., Vogt, M.T., Orwoll, E.S., Study of Osteoporotic Fractures Research, G., 2005. Hip fracture in women without osteoporosis. J Clin Endocrinol Metab 90, 2787-2793.

Wang, M.Y., Gao, X., Abdel-Wahab, A., Li, S.M., Zimmermann, E.A., Riedel, C., Busse, B., Silberschmidt, V.V., 2015. Effect of micromorphology of cortical bone tissue on crack propagation under dynamic loading. Epj Web Conf 94.

Wang, M.Y., Zimmermann, E.A., Riedel, C., Busseb, B., Li, S.M., Silberschmidt, V.V., 2017. Effect of micro-morphology of cortical bone tissue on fracture toughness and crack propagation. Xxvii International Conference: Mathematical and Computer Simulation in Mechanics of Solids and Structures - Fundamentals of Static and Dynamic Fracture (Mcm 2017) 6, 64-68.

Wegst, U.G., Bai, H., Saiz, E., Tomsia, A.P., Ritchie, R.O., 2015. Bioinspired structural materials. Nat Mater 14, 23-36.

Willett, T.L., Dapaah, D.Y., Uppuganti, S., Granke, M., Nyman, J.S., 2019. Bone collagen network integrity and transverse fracture toughness of human cortical bone. Bone 120, 187-193.

Wolfram, U., Schwiedrzik, J.J., Mirzaali, M.J., Burki, A., Varga, P., Olivier, C., Peyrin, F., Zysset, P.K., 2016. Characterizing microcrack orientation distribution functions in osteonal bone samples. J Microsc 264, 268-281.

Xu, X.P., Needleman, A., 1994. Numerical Simulations of Fast Crack-Growth in Brittle Solids. J Mech Phys Solids 42, 1397.

Yeni, Y.N., Norman, T.L., 2000. Calculation of porosity and osteonal cement line effects on the effective fracture toughness of cortical bone in longitudinal crack growth. J Biomed Mater Res 51, 504-509.

Zhai, X., Guo, Z., Gao, J., Kedir, N., Nie, Y., Claus, B., Sun, T., Xiao, X., Fezzaa, K., Chen, W.W., 2019. High-speed X-ray visualization of dynamic crack initiation and propagation in bone. Acta Biomater 90, 278-286.

Zhang, Z., Thompson, M., Field, C., Li, W., Li, Q., Swain, M.V., 2016. Fracture behavior of inlay and onlay fixed partial dentures - An in-vitro experimental and XFEM modeling study. J Mech Behav Biomed Mater 59, 279-290.

Zimmermann, E.A., Busse, B., Ritchie, R.O., 2015. The fracture mechanics of human bone: influence of disease and treatment. Bonekey Rep 4, 743.

Zimmermann, E.A., Gludovatz, B., Schaible, E., Busse, B., Ritchie, R.O., 2014. Fracture resistance of human cortical bone across multiple length-scales at physiological strain rates. Biomaterials 35, 5472-5481.

Zimmermann, E.A., Launey, M.E., Barth, H.D., Ritchie, R.O., 2009. Mixed-mode fracture of human cortical bone. Biomaterials 30, 5877-5884.

Zimmermann, E.A., Launey, M.E., Ritchie, R.O., 2010. The significance of crack-resistance curves to the mixed-mode fracture toughness of human cortical bone. Biomaterials 31, 5297-5305.

Zimmermann, E.A., Ritchie, R.O., 2015. Bone as a Structural Material. Advanced Healthcare Materials 4, 1287-1304.

Zimmermann, E.A., Schaible, E., Bale, H., Barth, H.D., Tang, S.Y., Reichert, P., Busse, B., Alliston, T., Ager, J.W., 3rd, Ritchie, R.O., 2011. Age-related changes in the plasticity and toughness of human cortical bone at multiple length scales. Proc Natl Acad Sci U S A 108, 14416-14421.

Zimmermann, E.A., Schaible, E., Gludovatz, B., Schmidt, F.N., Riedel, C., Krause, M., Vettorazzi, E., Acevedo, C., Hahn, M., Puschel, K., Tang, S., Amling, M., Ritchie, R.O., Busse, B., 2016. Intrinsic mechanical behavior of femoral cortical bone in young, osteoporotic and bisphosphonate-treated individuals in low- and high energy fracture conditions. Sci Rep 6, 21072.

Zioupos, P., 2001. Accumulation of in-vivo fatigue microdamage and its relation to biomechanical properties in ageing human cortical bone. J Microsc 201, 270-278.